7-22-2022

Using GMOS Spectroscopy to Study Star Formation and AGN in the CANDELS COSMOS and UDS Fields

Isabella G. Cox
igc5972@rit.edu

Using GMOS Spectroscopy to Study Star Formation and AGN in the CANDELS COSMOS and UDS Fields

ISABELLA G. COX

A Thesis Submitted in Partial Fulfillment of the Requirements for the Degree of Master of Science in Astrophysical Sciences & Technology

School of Physics and Astronomy
College of Science
Rochester Institute of Technology
Rochester, NY
July 22, 2022

Approved by: _____

Dr. Andrew Robinson — Date
Director, Astrophysical Sciences and Technology

ASTROPHYSICAL SCIENCES AND TECHNOLOGY
COLLEGE OF SCIENCE
ROCHESTER INSTITUTE OF TECHNOLOGY
ROCHESTER, NEW YORK

CERTIFICATE OF APPROVAL

MASTER'S DEGREE Thesis

The Master's Degree Thesis of *Isabella G. Cox* has been examined and approved by the thesis committee as satisfactory for the thesis requirement for the Master of Science degree in Astrophysical Sciences and Technology.

_____

Dr. Jeyhan Kartaltepe, Thesis Advisor

_____

Dr. Michael Lam, Committee Member

_____

Dr. Andrew Robinson, Committee Member

Date: _____

Abstract

Spectroscopic measurements of galaxies can help us to better understand their properties. Spectroscopy allows for the measurement of spectroscopic redshifts, which have better precision than redshifts derived from photometry. Precise redshifts are needed to eliminate distance uncertainties when deriving distance-dependent properties of galaxies. Additionally, spectroscopy provides insight into the physical state and processes within a galaxy, such as its rate of ongoing star formation, its chemical abundance, and the properties of the interstellar medium within the galaxy. Spectroscopy is particularly powerful when coupled with broad, multiwavelength photometric data. The five extragalactic fields from the Cosmic Assembly Near-infrared Deep Extragalactic Legacy Survey (CANDELS) have excellent multiwavelength photometric coverage. Two of the fields however, were lacking in spectroscopic coverage. To rectify this, spectroscopic observations were taken for sources in those particular fields in 2014, 2016, and 2019 with the Gemini Multi-Object Spectrometer on the twin Gemini Telescopes. We reduced the spectroscopic observations, which were taken in a configuration not compatible with existing reduction pipelines. We were able to extract spectra for 196 sources and measured their spectroscopic redshifts. We also measured emission fluxes from the spectra. We used the Hα and [OII]$_{\lambda 3727}$ emission lines as star formation rate indicators to measure the star formation rates of our galaxies, and compared these results to star formation rates obtained from other techniques. We also used Hβ, [OIII]$_{\lambda 5007}$, Hα, and [NII]$_{\lambda 6583}$ to construct diagnostics to detect AGN in our sample, and compared those classifications to sources in our sample detected as an AGN with other methods (e.g., mid-infrared colors, X-ray flux). Using the spectroscopic data, we identified seven possible AGN sources not identified with X-ray or infrared data that could be followed up.

Contents

1 Introduction **8**

1.1 Extragalactic Optical Spectroscopy 9

1.2 Spectroscopic Redshifts 12

1.3 The Effects of Dust 14

1.4 Spectral Energy Distribution Modeling 15

1.5 Star Formation Rates 17

1.5.1 UV Star Formation Rates 19

1.5.2 Far-Infrared Star Formation Rates 20

1.5.3 UV+FIR Star Formation Rates 20

1.5.4 SED Modeling Star Formation Rates 22

1.5.5 Rest Frame Optical Emission Line Star Formation Rates 22

1.6 Detecting AGN 24

1.6.1 X-ray AGN Detection 26

1.6.2 Infrared AGN Detection 26

1.6.3 Rest-Frame Emission Line AGN Detection 29

1.7 Motivation for Present Work 33

2 Data and Observations **34**

2.1 CANDELS Observations and Derived Data 34

2.2 X-ray Data 37

2.3 Mid- and Far-Infrared Data 38

2.4 Target Selection 38

2.5 GMOS Observing Strategy 40

3 Data Reduction and Processing **44**

3.1 Reduction Pipeline 44

3.2 Flux Calibration Technique 46

4 Analysis **47**

4.1 Measuring Redshifts 47

4.2 Measuring Emission Line Fluxes 49

4.3 Flux Attenuation Corrections and SED modeling 50

5 Results and Discussion **51**

5.1 Redshift Comparison and Completeness 51

5.2 Star Formation Rates 53

5.3 AGN Classifications 56

6 Summary and Conclusions **59**

A Appendix A **70**

List of Figures

1 An example optical spectrum of a star-forming galaxy (z = 0.16742) from SDSS. Emission lines are indicated with blue dashes, and are labeled with their names. Figure credit: SDSS Team, DR17 (Abdurro'uf et al., 2022). 10

2 The difference between extinction and attenuation. Left panel: A target star emits three beams of light, one of which is scattered by dust out of the line of sight, and the other two are reddened by the dust in the line of sight. Right panel: A target star emits a beam of light that passes through two dust clouds in the line of sight, redenning it. Other stars that exist in and around the line of sight are affected by the dust as well, as some of their light is redirected towards the viewer. Figure credit: Salim & Narayanan (2020). 15

3 An SED and best fit models from `MAGPHYS` for the nearby ($z = 0.0069$) galaxy NGC 3665. In the upper panel, the red circles are the measured photometric points for this galaxy. The black line is the best-fit attenuated model, and the blue line is the best-fit unattenuated model, which shows the stellar SED. The lower middle shows the residuals for the fit to each data point. The twelve lower panels shown the likelihood distribution for each of the properties returned by `MAGPHYS`, as discussed in Section 1.5.4. Figure credit: Xiao et al. (2018). 18

4 A comparision between SFRs computed with just the UV luminosity (y-axis) and SFRs computed with a calibration including UV and FIR luminosities (x-axis). The grey open circles represent UV SFRs from UV luminosities that were *not* corrected for attenuation and the black solid circles represent UV SFRs that used UV luminosities that were corrected for attenuation. The black dashed line represents the one-to-one line. Figure credit: Elbaz et al. (2007). 21

5 The total SFRs from UV+IR (black points) and SED modeling (grey points) as a function of the SFR from Hα. In all three subplots, the black line is the 1-1 line. The left-most panel shows Hα SFRs with no attenuation correction, the middle shows them with the correction from the SED output and the right panel shows the Hα SFRs with an additional attenuation correction calibrated to account for the extra dust obscuring HII regions. The Hα SFRs only come intro agreement with the total SFRs when the extra attenuation correction is applied. Figure credit: Wuyts et al. (2011). 23

6 A schematic of a slice through an AGN. The disk (dark blue), corona (cyan blue), and ionization cone (grey) are labeled, as well as the torus, the NLR and BLR. The coloring of the components shows which components contribute to the same parts of the SED of an AGN. Figure credit: Hickox & Alexander (2018). 25

7 11 composite MIR SED templates from Kirkpatrick et al. (2015). The offset in luminosity space is arbitrary for visualization purposes. The number in the legend label for each curve corresponds to the fractional amount of AGN contribution, so MIR0.0 has no AGN contribution and MIRI1.0 has 100% AGN contribution. Shaded regions indicate each template's uncertainties. MIR1.0 has a smoother positive slope over the the MIR range compared to templates with lower AGN fractions. Figure credit: Kirkpatrick et al. (2015). 27

8 In IRAC color-color space, the revised Donley et al. (2012) selection criteria establishes a selection wedge outlined in the thick black line. The thin black boundary is the selection criteria from Lacy et al. (2004); Lacy et al. (2007). The small points represent sources that do not fall within the Donley et al. (2012) selection wedge. The green points represent sources that were positively identified as an AGN with a different selection schema, Stern et al. (2005). The red (dark blue) points represent X-ray (non X-ray) sources classified with this approach as an AGN. The yellow points represent sources that do fall within the selection wedge, but do that have their IRAC bands increasing monotonically (see constraint 8a). Figure credit: Donley et al. (2012). 29

9 A BPT diagram for ∼85,000 emission-line galaxies from SDSS. The red solid line is the Kewley et al. (2001) line and is the theoretically-derived maximum starburst line. The black dashed line is the Kauffmann et al. (2003) line, which is a recalibration on the Kewley et al. (2001) based on observational data. The three separated regions are labeled. Figure credit: Kewley et al. (2006). 31

10 Left panel: A MeX diagram for SDSS sources. Sources classified as star-forming are colored purple, AGN sources are colored orange, and intermediate (composite) sources are colored blue. Right panel: A BPT diagram for the same sources as the left panel. The coloring is the same, with contours just for the star-forming and AGN classifications. Figure credit: Juneau et al. (2011). 32

11 The mask designs overlaid (red) on an F160W HST mosaic are shown for the three different observing programs. Note that we only show here the masks that were actually observed, and not just planned. Starting from the upper plot left and going clockwise, the corresponding GMOS program IDs are: GN-2014A-Q-10, GS-2019A-Q-219, GS-2014B-Q-23+GS-2016B-Q-18. 43

12 An example rest-frame spectrum for one galaxy, COSMOSJ100043.54+022524.27, with a measured spectroscopic redshift of $z = 0.7281$. The upper panel shows the reduced two-dimensional spectrum and the lower panel shows the extracted one-dimensional spectrum. The one-dimensional spectrum has been continuum subtracted and flux-calibrated as described in Section 3.2. Six emission lines are visible in both the one- and two-dimensional spectrum and were identified with the emission line fitting software `ALFA` (see Section 4.2). From increasing wavelength, the present emission lines are $[OII]_{3726,3729}$, $[NeIII]_{3869}$, Hγ, Hβ, $[OIII]_{4959}$, and $[OIII]_{5007}$. The [OII] doublet is not resolved in this example. 45

13 The stacked distributions of measured redshifts for COS (left panel) and UDS (right panel). The height of the area upper-bounded by black represents the number of high QF sources at each redshift, and the height of the area upper-bounded by red represents low QF sources. 48

14 This Venn diagram shows the number of each sources that have a particular combination of emission lines. The number in the outer part of each bulb shape indicates how many galaxies in total that had spectra with the labeled emission line detected at S/N > 3. The number in the overlapping shape regions indicate the number of sources that have the emission lines represented by the shapes being overlapped. For example, 36 sources have an Hα emission line, 75 have Hβ, 18 have $[\mathrm{NII}]_{\lambda 6583}$, 71 have $[\mathrm{OIII}]_{\lambda 5007}$, and 87 have $[\mathrm{OII}]_{\lambda 3727}$. Only nine galaxies have all four of those lines. Some regions contain a zero because there were no sources that contained all of those lines. 50

15 Upper panels: photometric redshift compared to spectroscopic redshift for the COS (left) and UDS (right) GMOS observations. The solid line represents the one-to-one line where points on that line represent sources that have the same photometric and measured spectroscopic redshift. Lower panels: the residuals between the photometric and spectroscopic redshifts, divided by $1 + \mathrm{z_{spec}}$. Dashed lines are used to demarcate boundary lines for outliers, which are defined as $|\mathrm{z_{spec}} - \mathrm{z_{phot}}| / (1 + \mathrm{z_{spec}}) > 0.15$. In both panels, sources with a low quality flag (QF = 1 or 2) are denoted by open shapes and sources with a high quality flag (QF = 3 or 4) are represented by closed shapes. For the left panel, we differentiate between sources from the 2014 run on GMOS-N and 2019 run on GMOS-S using a circle for the GMOS-N sources and a triangle for the GMOS-S sources. Note that there were no COS GMOS-S sources with a high quality flag. See Section 4.1 for a description of the quality flag system. 52

16 The fractional success rate (targets with measurable spectroscopic redshifts) are plotted for bins of I-band (F814W) magnitude for COS sources (left panel) and UDS sources (right panel). The I-band magnitudes of sources with high QF redshifts are shown in solid black and the I-band magnitude of sources with low QF redshifts are shown in dashed red. For the left panel, sources part of the two COS programs (GMOS-N COS and GMOS-S COS) are separated out, with sources from GMOS-S COS plotted in dot-dashed blue. All of the sources from GMOS-S COS were low QF sources. 53

17 The SFR for each source as estimated from optical emission line fluxes as a function of the corresponding SFR from SED modeling with `MAGPHYS` The salmon circle points are SFRs calculated with the Hα emission line fluxes and the the blue square points are from $[OII]_{\lambda 3727}$ fluxes. Open shapes represent the SFR as calculated with an emission line flux that was corrected for attenuation, as described in Section 4.3. The filled shapes are SFRs derived from emission lines not corrected for attenuation. The black dotted line represents the 1-1 line of equal SFR estimates for the line method and the SFR derived from SED modeling. 54

18 We show the SFRs as a function of stellar mass for three redshift ranges ($z < 0.5$, $0.5 < z < 1.0$, and $z > 1.0$, from the left to right panels). The coloring for the emission line SFRs is the same as Figure 17 and then the black diamonds are for the SFRs from the `MAGPHYS` SED modeling. The gray shaded area encompassess a factor of three above and below the main sequence, from Schreiber et al. (2015). 55

19 An optical diagnostic diagram (BPT) for the nine sources that have Hα, Hβ, [OIII], and [NII] measured emission line fluxes. The lower solid line is the semi-empirical line from Kauffmann et al. (2003), with star-forming galaxies lying below and to the left of this line. The dotted line is the maximum starburst line from Kewley et al. (2001), that marks the theoretical boundary separating AGN sources on the right. In between the two lines are the composite sources. The differently shaped colored points indicate the classification of a certain point from different AGN criteria, see Figure 20. 58

20 Left panel: The Mass Excitation (MeX; Juneau et al. 2011) including 63 of our sources. The ratio of $[\mathrm{OIII}]_{\lambda 5007}/H\beta$ is plotted as a function of stellar mass, which is a proxy for $[\mathrm{NII}]_{\lambda 6584}/\mathrm{H}\alpha$ which is used as the x-asis in a BPT Diagram. Identifications from other diagrams (Figure 19 and right panel of this Figure) are indicated by the legend. Right panel: The ratios of two IRAC bands are plotted against each other to identify IR AGN in this color space. The colored wedge indicates the region where AGN sources lie (Donley et al., 2012), and five of our sources are contained within there. Only one source, indicated with a red diamond, meets the full IR AGN criteria, including the monotonically increasing MIR slope. 59

List of Tables

1 Photometric data used from the COSMOS CANDELS catalog. The 5σ limiting depths come from Nayyeri et al. (2017). 36

2 Photometric data used from the UDS CANDELS catalog. The 5σ limiting depths come from Galametz et al. (2013). 37

3 A summary of the programs used in this thesis, including the names used to reference them, their associated Gemini program ID(s), the years they were observed, and the types of sources they targeted. 39

4 Observation summaries for the three programs, showing the program IDs, the number of slits observed, and the number of slits with actual detections, the dates of observations, the exposure time and the weather at the time of each observation. Weather comments came from the observing logs where possible. For GMOS-N observations without weather comments, we record the conditions from the SkyProbe instrument on the Canadian French Hawaii Telescope which is also on Mauna Kea where GMOS-N is. 42

5 Quality Flag Descriptions. 47

6 Quality Flag Breakdown by program. 48

7 The number of galaxies with S/N> $ss3$ detections for each emission line. 49

8 The properties of our sources, including identification information, the measured spectroscopic redshifts and their associated quality flags, and the SFRs and AGN classifications. We show the SFRs from the two emission lines we used, Hα and [OII]$_{\lambda 3727}$, which are the uncalibrated values (see Section 4.3 for a discussion on the attenuation corrections). We also show the AGN flags based on the four different classification systems we used, as discussed in Section 5.3. A value of 1 indicates that source was identified as an AGN with that detection technique, a value of 0 means that it was not, and the absence of a classification means that the necessary data for that technique was not available. 71

1 Introduction

A key area of interest for extragalactic astrophysicists is understanding the processes by which galaxies form and evolve. This involves looking at how galaxies form their stars, when and why they stop forming stars, and the looking at the properties of galaxies at all different stages of the evolutionary process.

Most galaxies cannot be clearly visualized from our vantage point, a result of either their large distance away or other restricting factors such as the presence of dust between us. It is also impossible for us to observe more than a snapshot of a galaxy's life. Evolutionary processes imprint information on the properties of galaxies. We can learn about the properties of galaxies such as their masses, star formation rates (SFRs), chemical compositions, etc. by making measurements of galaxies. These including imaging, measuring the amount of light through different filters (photometry), or dispersing the light through a prism to obtain a spectrum (spectroscopy).

Translating these observational measurements into measures of the physical properties of galaxies is a main objective of extragalactic astrophysics. Typically, measurements we make, such as the flux in a specific wavelength range, are scaled into physical properties through calibrations. Many of these calibrations are distant-dependent, because distance is required to convert the observed flux to the luminosity. The most accurate measurements of distance between us and a galaxy come from spectroscopy, as discussed in Section 1.2. For this reason, spectroscopy is a critical tool in our analysis of the properties of other galaxies. For similar reasons, spectroscopy is also critical for making measurements of the density of the environment that galaxies live in, whether that be a field-like environment where galaxies are spread far apart or a cluster where galaxies are existing in close proximity to other galaxies. Environmental density information is important for studies of how the properties of galaxies relate to their environment. Additionally, from spectra we can observe emission lines, which can give us information about the chemical composition of the galaxy from which the light came. We can also directly estimate physical properties from some of these emission lines, such as the star formation rate. Spectroscopy is a critical tool in our quest to understand the properties and evolution of other galaxies.

1.1 Extragalactic Optical Spectroscopy

The spectrum of a galaxy is not the result of an individual object, but rather is the composite spectrum of the stars and other baryonic components of a galaxy, such as gas and dust. We learn from the spectrum of a galaxy by studying the one or multiple features present: the continuum, absorption lines, and emission lines. The continuum sets the continuous overall shape, and is the result of total black-body radiation from thermally radiating matter such as the stars, gas, and dust inside the galaxy. Absorption and emission line features are a result of energy transitions within atoms and molecules. Absorption lines are the result of photons from the continuum spectrum interacting with atoms or molecules between their place of origin and the viewer. It is possible for atoms or molecules to absorb photons of specific energies corresponding to allowed energy level transitions, which will result in a dip in the spectrum at the corresponding wavelength. Emission lines are caused by photons emitted by atoms or molecules whose electrons drop to lower energy levels. We observe the result of this process as light emission at specific wavelengths. Figure 1 shows an example optical spectrum from the SDSS for a galaxy that is actively forming stars (Abdurro'uf et al., 2022). This galaxy has strong emission lines, including $[\mathrm{OII}]_{\lambda 3727,3729}$, $\mathrm{H}\beta$, $[\mathrm{OIII}]_{\lambda 5007}$, $[\mathrm{NII}]_{\lambda 654,\ \lambda 6583}$, and $\mathrm{H}\alpha$ as the strongest lines. In the spectrum, these emission lines occur at a different wavelength than they were emitted at, as a consequence of cosmological redshift as discussed in Section 1.2.

The three types of spectra (continuum, absorption lines, and emission lines) encode information about the physical properties of their source galaxies. Inferring useful information about a galaxy including its stellar mass, star formation rate (SFR), chemical composition, and metallicity from its spectrum usually involves using diagnostics. Diagnostics are single or sets of spectral features that can be used to estimate properties of galaxies. While spectra can be taken over any part of the electromagnetic spectrum, many ground based facilities have optical wavelengths spectrographs. Compared to observations with space-based facilities, ground-based observations are less expensive, and optical photons can easily pass through Earth's atmosphere. Studying the emitted, or rest-frame optical light of a galaxy is particularly useful because many diagnostics exist for optical

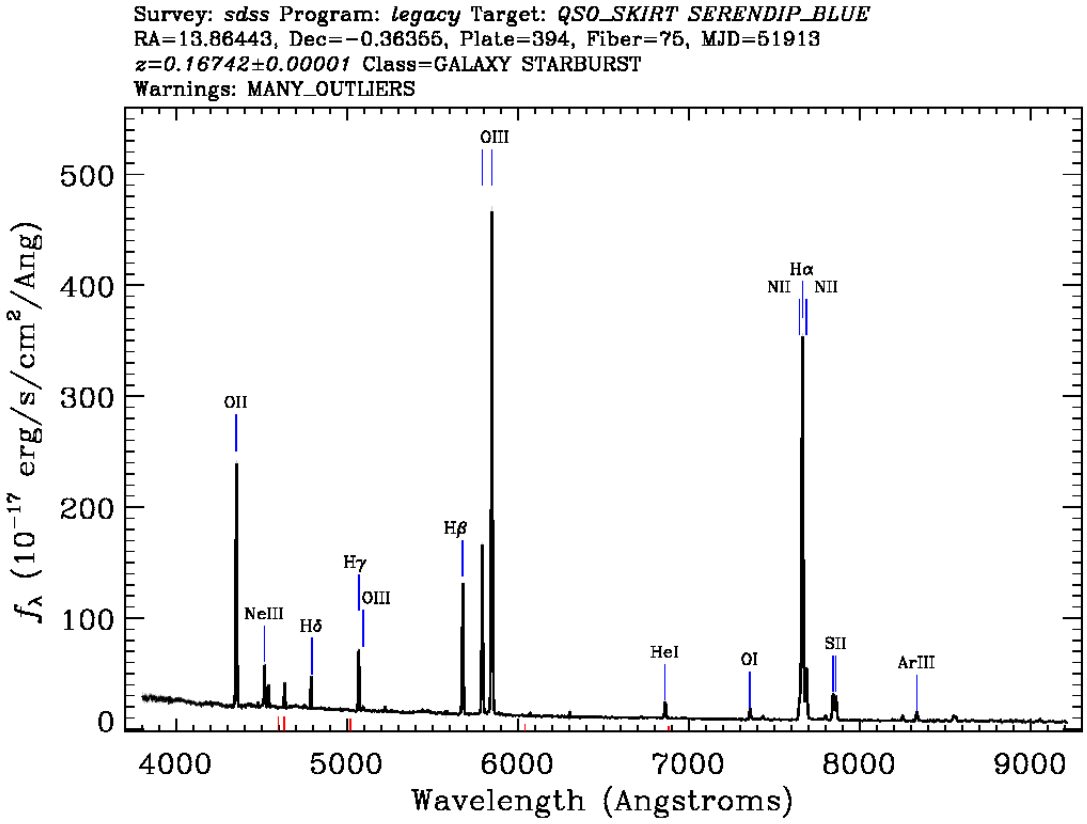

Figure 1: An example optical spectrum of a star-forming galaxy (z = 0.16742) from SDSS. Emission lines are indicated with blue dashes, and are labeled with their names. Figure credit: SDSS Team, DR17 (Abdurro'uf et al., 2022).

emission lines to study properties of a galaxy such as the SFR, chemical abundances or the dust present (Kewley et al., 2019). Optical spectroscopy is a powerful tool to help inform our understanding of the formation and evolution of galaxies because of the amount of information encoded within it that we can understand with diagnostics.

Large-scale rest-frame optical surveys started with the local Universe. Over 40 years ago, the original CfA survey was carried out at the Center for Astrophysics (CfA) at Harvard (Tonry & Davis, 1979). Since then, the collection and analysis of spectra have continued to occur, pushing out into studying deeper space. The Sloan Digital Sky Survey (SDSS) has been operational for

over 20 years, with the primary goal of obtaining photometric and spectroscopic data for sources across a large region of the sky (York et al., 2000). At the time of the current data release, DR17, optical spectra for almost half a million galaxies in the local Universe ($z \leq 0.1$) have been collected (Abdurro'uf et al., 2022). Studying the distribution of properties of galaxies has been possible with SDSS because of its large sample size. Results from analysis of SDSS data includes a clear demonstration that there is a bimodal distribution of properties between actively star-forming galaxies and more passive galaxies (Strateva et al., 2001). Another large local survey is the 2dF Galaxy Redshift Survey (Colless et al., 2001), which has recorded over 200,000 spectra for galaxies, with a median redshift of $z = 0.11$. Astrophysicists have used the accuracy of the spectroscopic redshifts from 2dF to map the density of galaxies. By having a precise constraint on the density of a galaxy's environment, it is possible to correlate the environment of a galaxy to its physical properties, such as luminosity and SFR (Norberg et al., 2002; Lewis et al., 2002). At higher redshifts, other surveys have been undertaken, such as DEEP2 ($z \leq 1$, $\sim$530,000 galaxies; Newman et al. 2013), and zCOSMOS ($z \leq 3$, $\sim$40,000 galaxies; Lilly et al. 2007). zCOSMOS was able to extend the study of the bimodality of galaxies' properties to a higher redshift than SDSS did (Pozzetti et al., 2010).

At redshifts greater than $z = 1.5$, observations with optical spectrographs probe shorter rest-frame wavelengths into the ultraviolet (UV), due to the expansion of the Universe. For ground-based studies that want to probe the rest-frame optical light of these sources, an obvious solution would be to use detectors designed for the longer wavelengths the optical light has been redshifted to. Ground-based near-infrared (NIR) spectrometers, exist, such as the MOSFIRE, an infrared instrument on the Keck telescope (McLean et al., 2012). Ground-based IR observations are challenging though, because IR photons are often absorbed by the upper atmosphere, preventing their observation from the ground. MOSFIRE and other ground-based IR detectors work by targeting specific redshift ranges where the desired emission lines will fall within narrow windows of transmissibility of the atmosphere. One solution is to go above the atmosphere, as was possible with the 2009 installation of the Wide Field Camera 3 (WFC3) on the *Hubble Space Telescope* (HST). With this new tool, the 3D-HST Survey (Momcheva et al., 2015; Brammer et al., 2012) recorded rest-frame optical

spectra for ∼250,000 galaxies, out to a redshift of $z = 6$, with tens of thousands of spectra recorded for galaxies at $z = 1 - 2$. However, these were low resolution grism spectra, meaning they were taken by adding a grating over an existing prism in a camera, which results in contamination from overlapping spectra of nearby sources. The NIRSpec instrument on the *James Webb Space Telescope* (JWST; Gardner et al. 2006) will be the first multi-object spectrograph in space, and will observe from 1 to 5μm.

1.2 Spectroscopic Redshifts

When astrophysicists observe the light from a galaxy, the *observed* light is at longer wavelengths than the intrinsic *emitted* light was. This phenomenon, referred to as redshift, is a direct consequence of the expansion of the Universe. From our (or any) vantage point, other galaxies are (generally) moving away from us and the speed at which they are moving away is proportional to their distance (Hubble, 1929). Ignoring the effects of relativity, which are relevant for galaxies with very large velocities, we define the quantity redshift, z, to be the ratio of the recessional velocity of a galaxy to the speed of light. The measurement of a redshift of a source can therefore yield its recessional velocity, which can be directly converted to a distance through Hubble's Law (Hubble, 1929). Distance is a parameter used when deriving many other physical quantities, and therefore accurate distances (from redshifts) are needed to avoid uncertainties propagating and enlarging through other calculations.

There are two techniques that are used to measure redshifts. Spectroscopic redshits are derived by comparing the wavelengths of observed emission or absorption lines to known laboratory values which are indicative of the emitted wavelength from the source. The wavelengths that emission lines of different species are emitted are well known as a result of laboratory studies. While the wavelength positions of emission lines shifts towards longer wavelengths as the result of cosmic expansion, the relative spacing between emission lines is unchanged by redshifting. This means that emission line groups can be identified in observed spectra, based on the characteristic spacing between them. Once the wavelength of a line in the emitted spectrum has been identified, that wavelength can be compared to the expected wavelength of the emitted line, and then used to

derive the redshift. The redshift is calculated as

$$z = \frac{\lambda_{obs} - \lambda_{emit}}{\lambda_{emit}}, \tag{1}$$

where the redshift value, z, is equal to the amount the observed wavelength of an emission line, λ_{obs}, is shifted from the wavelength it was emitted at, λ_{emit}, divided by λ_{emit}.

If there is not a spectrum available for an object, there is a second technique to estimate the redshift using photometry. Photometric redshifts uses the photometry of a galaxy to determine the redshift. Photometric filters gather light from a specific range of wavelengths. This means that photometry cannot differentiate between individual spectral features. However, it is still sensitive to the general shape of the continuum, and strong features, such as strong emission lines, or breaks in a spectrum, such as the 4000Å break or the Balmer break (Bolzonella et al., 2000). Spectral breaks are places in a spectrum where the intensity rapidly changes in a step-wise fashion. Capturing a strong feature within a photometric filter would have the effect of making the flux within that filter to be much larger or smaller than the fluxes through filters that cover neighboring wavelengths. A common way to translate this information into a redshift is to construct a spectral energy distribution (SED) with the data, which is a plot of the flux through each filter as a function of the filters' central wavelengths. This SED can then be compared to a library of template SEDs with known redshifts, and the galaxy is assumed to have the same redshift as the best-fitting template SED. This is not always a precise process, and it gets worse with the fewer photometric points that are used to construct the SED. If there are only a few photometric points available and there are not many (or any) neighboring filters used, a spectral feature could be mistaken for one that occurs at a different wavelength, and result in an innacurate redshift (Bolzonella et al., 2000).

Photometric redshifts are generally less accurate than spectroscopic redshifts so they are not preferred where spectroscopic redshifts are available. However, photometric redshifts can make use of photometry that covers tens of thousands of galaxies at once, so it is still used as a coarse measurement valuable for larger samples than can easily be covered with spectroscopy. The precision of photometric redshifts is also affected by how faint the target galaxy is. For the 966,000 galaxies

in the Cosmic Evolution Survey (COSMOS; Scoville et al. 2007) that had photometric redshifts measured using $\sim$ 44 photometrc bands, the precision of derived redshifts was found to be $< 1\%$ for the brightest sources ($\mathrm{mag_{AB}} < 21$) and increase to $\sim$5 % for the fainter sources ($\mathrm{mag_{AB}} > 25$) (Weaver et al., 2022).

1.3 The Effects of Dust

Dust grains exist throughout interstellar space, and can affect how much of the emitted light we detect as an observer. Dust can affect the light output by a galaxy in two ways. In the first way, dust can absorb light emitted in the UV and optical wavelengths and then re-radiate that energy in the infrared (Li, 2008). So in this way, dust can result in radiation from a galaxy at longer wavelengths than would occur were no dust to be present. The second way dust affects light is by scattering or absorbing emitted light, preferentially affecting shorter (bluer) wavelengths (Trumpler, 1930). The phenomenon of blue light being extinguished more than red light is referred to as "interstellar reddening." In order to understand the true nature of the intrinsic light of a galaxy, it is imperative to correct for the obscuring dust along the line of sight. Commonly, astrophysicists describe these corrections as rectifying the effects of "extinction" or the light lost along the line of sight due to dust present that is absorbing or scattering away the light. Extinction from dust has a wavelength dependence, where the amount that starlight is extinguished gets larger for wavelengths decreasing from IR to UV wavelengths (Draine, 2003).

The presence of dust introduces more factors beyond just absorbing and scattering. Dust can also cause starlight to be scattered back *into* the line of sight. Including this additional possibility, we refer to all of these effects of dust together as "attenuation." Attenuation includes the distribution of dust not just within the line of sight but also around it. And attenuation also accounts for the possibility of starlight coming from a different source than what is being observed entering the line of sight. Figure 2 is a graphical depiction of the difference between extinction and attenuation.

To correct for attenuation, curves of the amount of attenuation as a function of wavelength are used, typically derived with computer models (Salim & Narayanan, 2020). The most common model for simulating attenuation is the two-component model from Charlot & Fall (2000), which assumes

Figure 2: The difference between extinction and attenuation. Left panel: A target star emits three beams of light, one of which is scattered by dust out of the line of sight, and the other two are reddened by the dust in the line of sight. Right panel: A target star emits a beam of light that passes through two dust clouds in the line of sight, redenning it. Other stars that exist in and around the line of sight are affected by the dust as well, as some of their light is redirected towards the viewer. Figure credit: Salim & Narayanan (2020).

that all stars in a galaxy are subject to attenuation by the surrounding interstellar medium (ISM), but that young stars are also additionally attenuated by their surrounding birth clouds. This model was developed to match observations by Calzetti et al. (1994) which found additional attenuation along sight lines towards new stars within a galaxy.

1.4 Spectral Energy Distribution Modeling

Understanding the effects of dust is particularly important for fitting the SED of a galaxy. The shape of the SED of a galaxy is determined by the physical processes within a galaxy, such as its historical record of star formation, the current total stellar mass, and the amount of gas and dust present (Conroy, 2013). Since the SED encodes all of that information, it is possible to recover the values of unknown physical properties of a galaxy from it. The method to extract physical properties from an SED involves modeling the continuous SED of a galaxy using a library of models and then assuming that the galaxy has the same physical properties as the best-fit model SED does.

The models used for fitting SEDs are called "composite stellar populations" (CSPs) because they represent the combined SED of a population of stellar components. CSPs are constructed

from simple stellar population (SSP) models that are coupled with the additional information of dust attenuation and dust emission and models of the star formation and chemical evolution over the lifespan of the components of the SSPs (Conroy, 2013).

An SSP is the base unit of any SED modeling code. An SSP describes the SED of a single population of co-evolving stars with a fixed metallicity and chemical abundance pattern. The three "ingredients" for building an SSP are: stellar isochrones, stellar spectra, and an initial mass function (IMF). Stellar isochrones depict the location on a Hertzsprung-Russell (HR) diagram where stars of the same age and metallicity would be. Isochrones are determined for stars of a range of masses, and the mass parameter space is sampled finely enough to ensure smooth evolutionary transitions (Charlot & Bruzual, 1991). No single existing sets of isochrones (e.g., Bertelli et al. 1994; Girardi et al. 2000; Marigo et al. 2008; Pietrinferni et al. 2004; Schaller et al. 1992; Meynet & Maeder 2004; Chabrier & Baraffe 1997) individually span the full range of stellar properties. Therefore, it is common to combine sets. The second ingredient for develping an SSP are stellar spectra. Stellar spectral libraries contain spectra of stars, which are the building blocks of galaxies. Spectra are developed for stars across a wide range of evolutionary stages, temperatures, metallicities, etc. The stellar spectral library can either be developed empirically or theoretically. While empirical libraries have the benefit of being based on real stars, dense sampling over the full parameters space is difficult due to observational constraints (Leitherer, 2005). The final piece to construct an SSP is the IMF. The IMF is a distribution function for the initial masses of stars present. Generally, astrophysicists make the assumption the IMF is universal, although recent work has shown that may not be true (see for example: Bastian et al. 2010; Cappellari et al. 2012). The choice of assumed IMF can have effects on the properties measured for a galaxy. As an example, if the low-end mass of the IMF were assumed to be larger than it really were, stellar masses derived from photometry dependent on the IMF would be artificially larger, since most of the mass in stars comes from low-mass stars (Madau & Dickinson, 2014). However, using a universal IMF would most likely still preserve subsequently derived property values for galaxies relative to each other. Common IMF choices include the Salpeter IMF (Salpeter, 1955), which is a power law, the Kroupa IMF (Kroupa, 2001), which is a broken power law, and the Chabrier IMF (Chabrier, 2003), which is a log-normal

trend.

The previously described workings of the process of SED modeling are typically in a "black box" for users (Conroy, 2013). Most SED modeling codes work by accepting the user-inputted SED of a galaxy, and then returning the best fit model SED and the associated properties of that model (and thus, the assumed properties of the inputted galaxy). Many SED modeling codes exist, an incomplete list includes `LePHARE` (Arnouts et al., 1999; Ilbert et al., 2006), `CIGALE` (Burgarella et al., 2005; Noll et al., 2009; Boquien et al., 2019), `Prospector` (Johnson et al., 2021), `BAGPIPES` (Carnall et al., 2018), `EAZY` (Brammer et al., 2008), and `MAGPHYS` (da Cunha et al., 2011).

In this thesis, we use `MAGPHYS`, which uses energy balance to make sure that the modeled IR emission is consistent with the emission from the UV and optical. Some of the emission from the UV and optical wavelengths is absorbed by dust in galaxies, and then processed and re-radiated by the dust as thermal radiation in the IR. `MAGPHYS` ensures that the amount of emission from the IR in its models is physically appropriate for the amount of emission that was originally output at shorter wavelengths. Figure 3 shows an example SED with a the best-fit models from `MAGPHYS`. As described in Section 5, we used the properties of the best-fit models from running `MAPGHYS` on the SEDs of our sources in our analysis.

1.5 Star Formation Rates

The SFR of a galaxy is the mass of stars formed per unit of time (typically expressed in solar masses per year). Ideally, one would measure the SFR by looking for direct objects or events (e.g., supernovae) indicative of star formation. However, this strategy is only possible for highly resolved, nearby systems, such as parts of our own Milky Way Galaxy (e.g., Chomiuk & Povich 2011). For the majority of extragalactic sources studied, one must rely on *indirect* metrics of star formation. So-called SFR indicators generally work by scaling a luminosity to a SFR. That luminosity may be monochromatic, or integrated over a wavelength range.

An indicator ideally will target light emitted by the short-lived, young massive stellar population. The luminosity measured can be converted into the number or mass of these stars. Using an estimated distribution of stellar masses (from the IMF), the census of other young, though less-

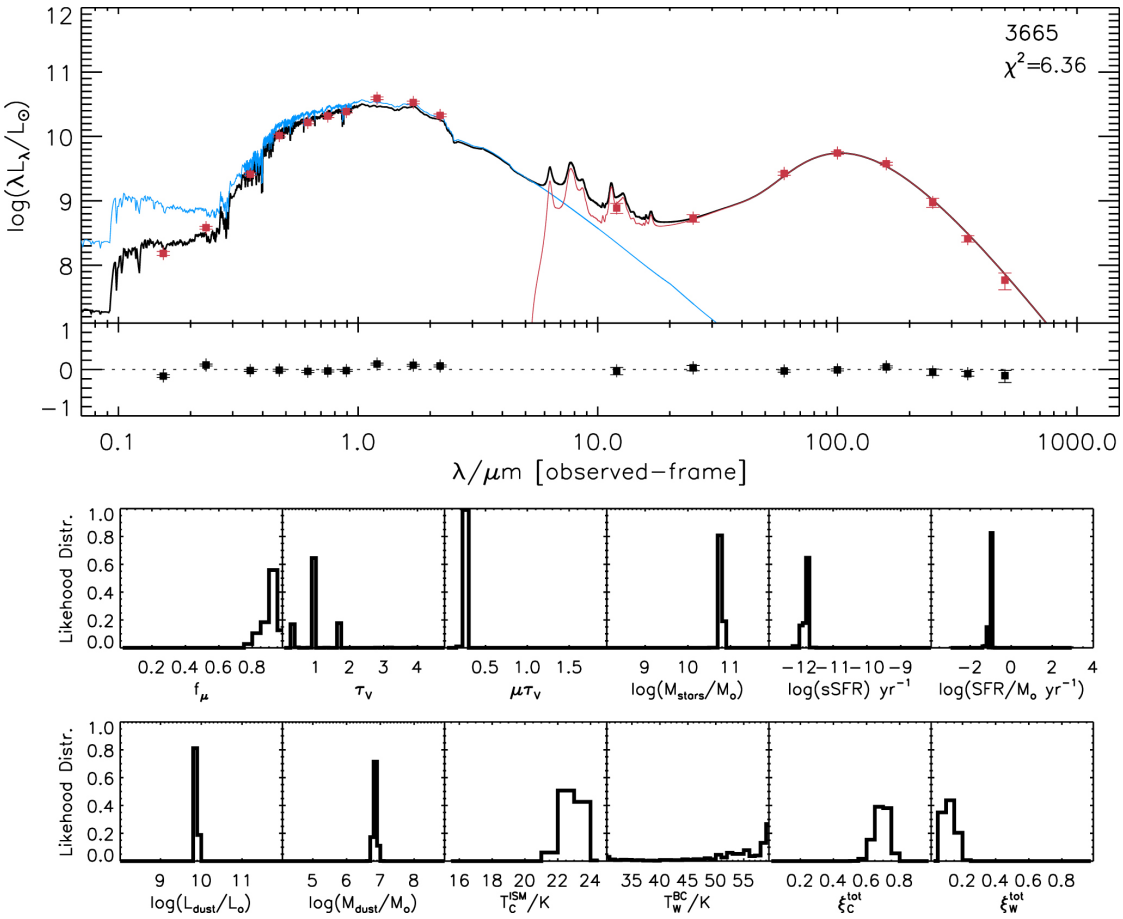

Figure 3: An SED and best fit models from `MAGPHYS` for the nearby ($z = 0.0069$) galaxy NGC 3665. In the upper panel, the red circles are the measured photometric points for this galaxy. The black line is the best-fit attenuated model, and the blue line is the best-fit unattenuated model, which shows the stellar SED. The lower middle shows the residuals for the fit to each data point. The twelve lower panels shown the likelihood distribution for each of the properties returned by `MAGPHYS`, as discussed in Section 1.5.4. Figure credit: Xiao et al. (2018).

massive stars can be extrapolated. Finally, the total mass of these stars is divided by the presumed timescale over which they grew, to provide a star formation rate. This process heavily relies on models of populations of stars, and applies the results of such modelling into the conversion (Calzetti, 2012). SFR indicators have been calibrated across the electromagnetic spectrum, and are well-defined from the UV to FIR (see for example: Kennicutt 1998; Kewley et al. 2004, 2002; Calzetti et al. 2005, 2007, 2010; Rosa-Gonzá lez et al. 2002).

1.5.1 UV Star Formation Rates

Emission from the near-UV in galaxies directly traces emission from very young stars, and therefore provides one of the best estimates of current star formation. Emission from the UV traces stars over short timescales, 10-200Myr (Kennicutt & Evans, 2012). UV observations must be taken from the Earth's upper-atmosphere or space-based observatories, as UV light is largely absorbed by the atmosphere. Observations from the Galaxy Evolution Explorer (GALEX; Martin et al. 2005) and the *Hubble Space Telescope* (HST) have been instrumental in collecting integrated UV fluxes for hundreds of thousands of galaxies that could be converted into SFRs (Kennicutt & Evans, 2012). The conversion from UV luminosity to SFR from Rosa-Gonzá lez et al. (2002) is,

$$\mathrm{SFR_{UV}}\ [\mathrm{M_\odot\ yr^{-1}}] = 1.4 \times 10^{-28} \mathrm{L_\nu}\ [\mathrm{erg\ s^{-1}\ Hz^{-1}}], \tag{2}$$

where L_ν is a UV luminosity per unit frequency within the wavelength range 1500 - 2800 Å and a Salpeter IMF is assumed.

Other than requiring space-based observations, the UV's largest drawback is its extreme sensitivity to interstellar extinction from dust. The most ideal way to correct for the interstellar extinction would be to compare an observed far-UV (FUV)–NUV color to the intrinsic FUV–NUV color to determine the amount of extinction. However, the accuracy of this correction is strongly dependent on the accuracy of the estimated intrinsic color, which cannot be known with complete certainty (Gordon et al., 2001). Due to the challenges and uncertainties in correcting for the effects of dust for UV observations, the UV SFRs are often not solely relied on and instead are coupled

with results from IR data (Kennicutt & Evans, 2012).

1.5.2 Far-Infrared Star Formation Rates

The FIR does not directly trace the emission of young stars. Rather, emssion in the FIR comes from radiation emitted at shorter wavelengths (mainly UV and optical) that was absorbed and then re-radiated by dust. This means that the amount of radiation output in the FIR is indicative of how much radiation the galaxy was originally emitting from stellar components. Instead of using a monochromatic IR luminosities, astrophysicists typically use a bolometric FIR luminosity, defined as the integrated luminosity from 8 to 1000μm. A single band cannot sample the full FIR SED, so an integrated luminosity is needed to capture all of the emission. Since a bolometric FIR luminosity would include light absorbed and re-radiated by dust at a range of UV and optical wavelengths, this measure of SFR would be over a longer timescale, as it would not include just the newest stars (Calzetti, 2012). The conversion from FIR luminosity to SFR from Kennicutt (1998) is,

$$\mathrm{SFR_{FIR}}\ [\mathrm{M_\odot\ yr^{-1}}] = 4.5 \times 10^{-44} \mathrm{L_{FIR}}\ [\mathrm{ergs\ s^{-1}}], \tag{3}$$

where L_{FIR} is the total bolometric IR luminosity. In cases where the total IR luminosity is not available, the luminosity for a single IR band (e.g., $\mathrm{L}_{60\mu m}$; see Chapman et al. 2000).

1.5.3 UV+FIR Star Formation Rates

As discussed in Section 1.5.1, dust attenuation has a major impact on the UV luminosity we observe from a galaxy, which could potentially affect the accuracy of the SFRs derived from UV luminosity. Similarly, FIR SFRs are also plagued by the potential problem that they are underestimating the total amount of star formation if less of the UV light than anticipated is being absorbed and re-emitted in the FIR because there is not that much dust present (Madau & Dickinson, 2014). To counteract both of these problems, the UV and FIR luminosities can be calibrated to be used as a combined SFR indicator. The combined conversion from the UV+FIR luminosities from Calzetti (2012) is,

$$\mathrm{SFR_{UV+FIR}}\ [\mathrm{M_\odot\ yr^{-1}}] = 4.6 \times 10^{-44}\,(\mathrm{L_{UV}} + 0.46\mathrm{L_{FIR}})\,[\mathrm{erg\ s^{-1}}], \quad (4)$$

where L_{UV} is the UV luminosity at 1530 Å (FUV) that is *not* corrected for dust attenuation and L_{FIR} is the bolometric FIR luminosity as described in Section 1.5.2. This calibration assumes a Kroupa IMF.

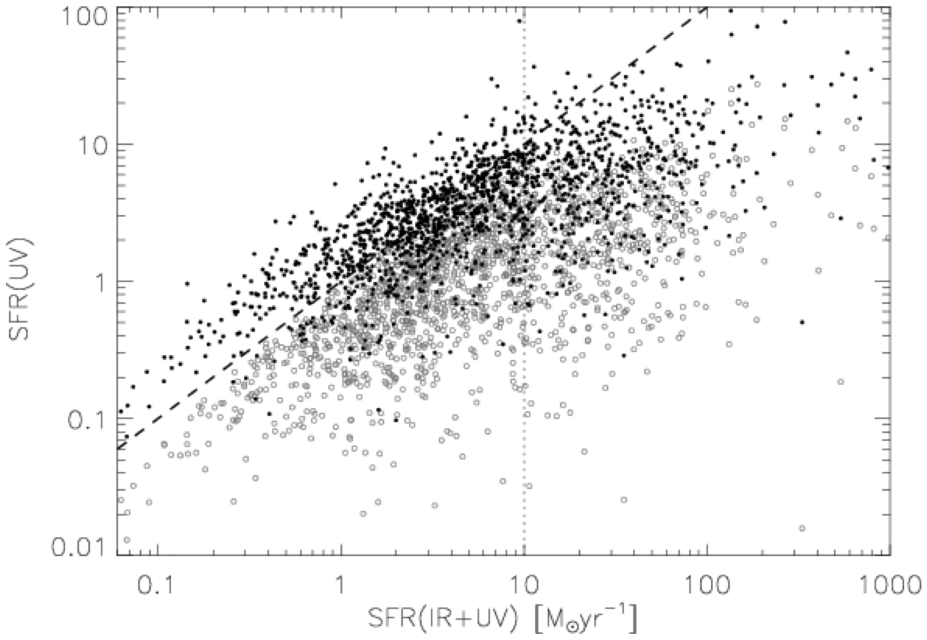

Figure 4: A comparision between SFRs computed with just the UV luminosity (y-axis) and SFRs computed with a calibration including UV and FIR luminosities (x-axis). The grey open circles represent UV SFRs from UV luminosities that were *not* corrected for attenuation and the black solid circles represent UV SFRs that used UV luminosities that were corrected for attenuation. The black dashed line represents the one-to-one line. Figure credit: Elbaz et al. (2007).

Figure 4 shows how the solely-UV SFR compares to the UV+FIR SFR for a sample of $\sim$ 1200 galaxies at redshift $0.8 \leq z \leq 1.2$. UV SFRs are included for both calibrations that used UV luminosities that had been corrected and not corrected for the effects of dust attenuation. UV SFRs that used UV luminosities corrected for attenuation have a much better agreement with the UV+IR SFRs. UV SFRs that did not use UV luminosities corrected for attenuation were generally

smaller than UV+IR luminosities by up to a factor of 10, which shows the strong attenuating effects that dust has on observed UV luminosities. Many of the UV SFRs from UV luminosities corrected for attenuation still lay below the 1-1 line. This is because the UV is more of an instantanous SFR that is sensitive to a shorter timescale than the UV+FIR SFR.

1.5.4 SED Modeling Star Formation Rates

SED modeling codes can return the estimated total SFR (among other properties) of a galaxy. In the modeling code `MAGPHYS`, specifically the best property values are determined by weighing the values of each parameter from the i^{th} model by the probability $\exp(-\chi_i^2/2)$ to construct a probability density function (PDF) and then picking the median value (da Cunha et al., 2011). Most SED fitting codes work very similarly though, by constructing a PDF and then choosing the best parameter value as the median. The lower panel of Figure 3 shows the likelihood distributions for the properties of a galaxy based on the `MAGPHYS` fitting code. The SFR distribution is shown as the upper right subplot in the lower panel of the figure. For this example galaxy, the SFR would be $\sim 10^{-1.5}$ $M_\odot$ yr^{-1}. The SFR that `MAGPHYS` returns is the SFR averaged over the past 10^8 years, so this SFR captures a longer timescale than more instantaneous measures, such as UV alone (da Cunha et al., 2011).

1.5.5 Rest Frame Optical Emission Line Star Formation Rates

Two optical emission lines, Hα and $[\text{OII}]_{\lambda 3727}$, are commonly used as SFR indicators. Hα is an excellent indicator for star formation, as it directly correlates to the the radiation produced by young, massive stars, which output radiation that ionize hydrogen.

We use the following relation for a Hα SFR from Kennicutt (1998):

$$\text{SFR}_{\text{H}\alpha}\ [\text{M}_\odot\ \text{yr}^{-1}] = 0.63 \times 7.92 \times 10^{-42} \text{L}(\text{H}\alpha)\ [\text{erg s}^{-1}\ \text{cm}^{-2}\ \text{Å}^{-1}], \tag{5}$$

which has been scaled to a Chabrier IMF for an unbiased comparision to results from `MAGPHYS`, which uses a Chabrier IMF, in this thesis. We multiplied the original relation by 0.63 to convert

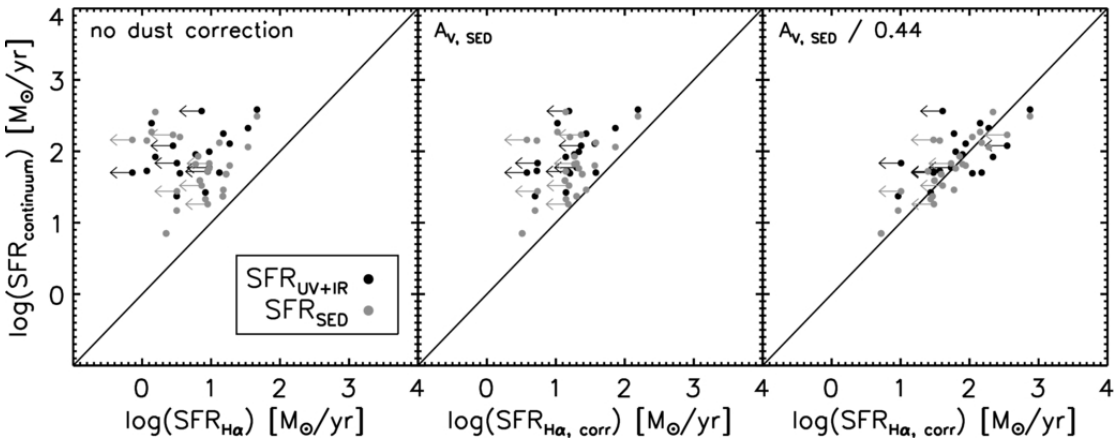

Figure 5: The total SFRs from UV+IR (black points) and SED modeling (grey points) as a function of the SFR from Hα. In all three subplots, the black line is the 1-1 line. The left-most panel shows Hα SFRs with no attenuation correction, the middle shows them with the correction from the SED output and the right panel shows the Hα SFRs with an additional attenuation correction calibrated to account for the extra dust obscuring HII regions. The Hα SFRs only come intro agreement with the total SFRs when the extra attenuation correction is applied. Figure credit: Wuyts et al. (2011).

from the Salpeter IMF to a Chabrier (Madau & Dickinson, 2014).

Since Hα is only observable at low redshifts ($z < 0.4$) with optical instruments, $[\mathrm{OII}]_{\lambda 3727}$ is another line that can be used to estimate the star formation rate of a galaxy. The $[\mathrm{OII}]_{\lambda 3727}$ measured flux is not directly proportional to the SFR, but it can be calibrated using Hα, either empirically (e.g., Rosa-Gonzá lez et al. 2002; Kewley et al. 2004) or theoretically (e.g., Charlot & Longhetti 2001).

We use the following relation for the $[\mathrm{OII}]_{\lambda 3727}$ SFR from Kennicutt (1998),

$$\mathrm{SFR}_{[\mathrm{OII}]}\ [\mathrm{M}_\odot\ \mathrm{yr}^{-1}] = 0.63 \times 1.40 \times 10^{-41} \mathrm{L}([\mathrm{OII}])\ [\mathrm{erg\ s}^{-1}\ \mathrm{cm}^{-2}\ \text{Å}^{-1}]. \quad (6)$$

which was scaled to a Chabrier IMF as described above. [OII] SFRs are commonly less-preferred, as systemic uncertainties are known to occur due to the dependence of the $[\mathrm{OII}]_{\lambda 3727}$ flux strength on dust, chemical abundance, and ionization which can vary broadly between galaxies (Moustakas et al., 2006). However, $[\mathrm{OII}]_{\lambda 3727}$ is still useful as an indicator for SFR when Hα is not present and also to include in comparisons of multiple SFR indicators.

Emission line SFRs like Hα tend to underestimate the total SFR of a galaxy, because they only trace the most current star formation. Figure 5 shows the comparision between total SFR measurements (from an SED and the UV+FIR) as a function of Hα SFRs, for a sample of moderate redshift star-forming galaxies. With no attenuation correction, the Hα SFRs are up to a factor of two smaller than the total SFRs. A discrepancy exists even when applying the attenuation correction from the SED output. The Hα SFRs are only brought into agreement with the total SFRs when the attenuation correction is increased to reflect the expected extra attenuation towards HII regions (Wuyts et al., 2011).

1.6 Detecting AGN

Active galactic nuclei (AGN) are the compact regions in the central parts of galaxies that have enhanced emission, typically over large parts of the electromagnetic spectrum. This emission does not come from stars, but is rather a result of mass accreting onto a supermassive black hole (SMBH; $M_\bullet \geq 10^6 M_\odot$) (Hickox & Alexander, 2018). The widely accepted physical model of AGN describes the accretion disk, which is the optically thick region generated by the accretion onto the SMBH (Shakura & Sunyaev, 1973; Novikov & Thorne, 1973) as emitting thermal radiation, and being surrounded by a dusty torus region (name given for the geometric shape describing its configuration). The anisotropic nature of the torus means that radiation from the accretion disk can only be directly detected through specific sight lines, and through others is obscured by the dusty torus (Hickox & Alexander, 2018). Also of consideration are the two different line emitting regions of an AGN: the narrow line region (NLR) and the broad line region (BLR). Surrounding the core of an AGN are clouds of gas. The gas in these clouds is photoionized by power-law continuum emission produced by the AGN, which results in the presence of emission lines in the observed spectrum. Commonly, these clouds of gas are thought of as two separate regions. The NLR is viewable for any AGN as it includes clouds outside of the dusty torus. Closest to the center of the black hole is the BLR. In the BLR, the velocity of the gas is rapid (typically at least 3,000 km/s) which results in Doppler broadening of lines in the observed spectrum (Peterson, 2006). At certain viewing angles of an AGN that cut through the torus, emission from the BLR is not viewable because it is obscured

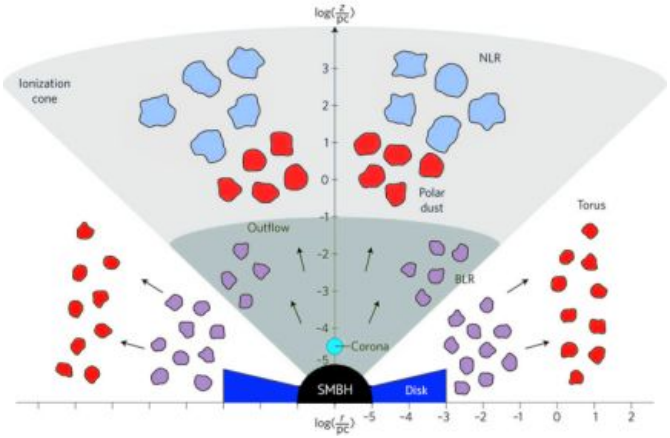

Figure 6: A schematic of a slice through an AGN. The disk (dark blue), corona (cyan blue), and ionization cone (grey) are labeled, as well as the torus, the NLR and BLR. The coloring of the components shows which components contribute to the same parts of the SED of an AGN. Figure credit: Hickox & Alexander (2018).

by the dust in the torus. AGN can also be obscured by dust present anywhere along the line of sight between it and the viewer, but most commonly are obscured by dust within the torus, for an orientation where the viewer's sight line is through the torus (**?**). This model is referred to as the "Unification Model" because it *unifies* the observed properties of different classes of AGN as being a consequence of the viewing angle into the AGN (Antonucci, 1993; Urry & Padovani, 1995). However, there are additional variables to consider rather than just orientation, such as the black hole's accretion rate, the host galaxy's properties and the strength of any present relativistic jets. A schematic of an AGN is shown in Figure 6, which labels the NLR, the BLR, the torus, the accretion disk, and the corona.

The accretion disk of an AGN emits thermally over a range of temperatures, which correspondingly produces emission over a range of wavelengths (Hickox & Alexander, 2018). This means that AGN can be detected with many different multiwavelength techniques. Some useful wavelength regimes to use include the IR, which is sensitive to the dust in the torus region, the optical, which traces emission from the accretion disk and the X-ray, which is thought to indicate the presence of the presumed coronal component (Padovani et al., 2017). However, in isolation, a specific technique is not infallible, as individually they are sensitive to different types of AGN, evolutionary stages,

orientations, etc. This is why multiwavelength analysis is necessary to identify the complete census of AGN.

1.6.1 X-ray AGN Detection

A common challenge in identifying AGN is to parse out what is a true AGN from a look-alike galaxy undergoing enhanced rates of star formation. Like AGN, star-forming galaxies can emit in the X-ray regime, which is emitted from ionized sub-keV gas around star-forming regions (Li & Wang, 2013; Tyler et al., 2004). Galaxies that are actively star-forming have more of this emission. However, a given AGN almost surely surpasses the energy output of a star-forming galaxy in X-ray part of the electromagnetic spectrum (Donley et al., 2012). This makes X-ray observations a useful tool for identifying AGN, and distinguishing them from non-AGN starforming galaxies. Sources with X-ray luminosities greater than 10^{42} erg s^{-1} are classified as X-ray AGN (Brandt & Alexander, 2015). This luminosity threshold ensures that the emission is dominated by an AGN and exceeds the luminosity that would be expected for a star-forming galaxy.

However, most X-rays observations are unable to detect obscured AGN (Treister et al., 2006). Modeling of the Cosmic X-ray background suggests that these highly obscured AGN constitute a significant fraction of the total AGN population (Gilli et al., 2006), and potentially missing them with X-ray observations means that a complete census of AGN is not possible with X-ray data alone. Regardless, X-ray still provides a useful way to detect AGN, particularly as a first pass for large surveys with wide X-ray coverage. Additionally, X-ray detected AGN are conclusively true AGN, whereas that assurance is not always possible with other AGN detection techniques.

1.6.2 Infrared AGN Detection

As described in Section 1.5.1, X-ray searches for AGN can miss the most obscured systems. An alternative method for searching for potentially obscured (and unobscured) AGN is to use the mid-infrared (MIR). AGN have a distinct slope in the MIR part of their SED compared to normal galaxies. Normal galaxies typically exhibit a dip in the MIR region of their SED. For AGN, there is no such dip as it has been "filled in" by MIR emission from the dusty torus (Donley et al., 2012).

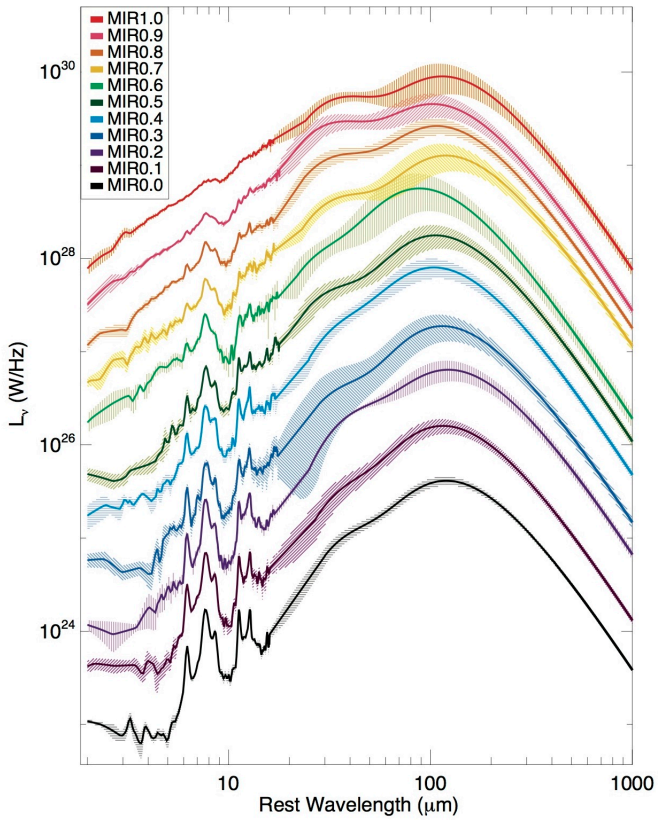

Figure 7: 11 composite MIR SED templates from Kirkpatrick et al. (2015). The offset in luminosity space is arbitrary for visualization purposes. The number in the legend label for each curve corresponds to the fractional amount of AGN contribution, so MIR0.0 has no AGN contribution and MIRI1.0 has 100% AGN contribution. Shaded regions indicate each template's uncertainties. MIR1.0 has a smoother positive slope over the the MIR range compared to templates with lower AGN fractions. Figure credit: Kirkpatrick et al. (2015).

.

Figure 7 shows example composite SEDs for galaxies with different degrees of AGN contribution. Galaxies with a a higher AGN fraction have a more smoothly increasing slope over the wavelength range from 1 to 10μm compared to galaxies with weaker AGN features, which have a dip over that same wavelength range. Often, the whole MIR SED is not available, so it is common to use color cuts to identify AGN. This technique works by enforcing criteria that define boundaries on a color-color diagram separating out AGN from other sources. Selection criteria must be liberal enough to have a high success rate in identifying AGN while still strict enough to exclude non-AGN

sources.

Previous work to select AGN with IR colors (see: Lacy et al. 2004; Lacy et al. 2007; Stern et al. 2005) produced selection cuts that could not be applied to higher redshifts due to contamination with star-forming galaxies in the selection areas. Donley et al. (2012) used a large sample of both AGN and higher redshift star-forming sources to empirically readjust the constraining boundaries to only include AGN in the selection area of the IRAC color-color diagram, even for higher redshifts. Figure 8 shows the wedge that the selection criteria constrain in the IRAC color-color space.

The Donley et al. (2012) selection criteria used data from the four MIR bands (3.6, 4.5, 5.8, and 8.0μm) on the Infrared Array Camera (IRAC) on the *Spitzer Space Telescope*. Defining the IRAC colors in log space as follows:

$$\mathrm{x} = \log_{10}\frac{\mathrm{f}_{5.8\mu\mathrm{m}}}{\mathrm{f}_{3.6\mu\mathrm{m}}}, \quad \mathrm{y} = \log_{10}\frac{\mathrm{f}_{8.0\mu\mathrm{m}}}{\mathrm{f}_{4.5\mu\mathrm{m}}} \tag{7}$$

,

the selection criteria are as follows:

$$\mathrm{f}_{8.0\mu\mathrm{m}} > \mathrm{f}_{5.8\mu\mathrm{m}} > \mathrm{f}_{4.5\mu\mathrm{m}} > \mathrm{f}_{3.6\mu\mathrm{m}} \tag{8a}$$

$$\mathrm{x} \geq 0.08 \tag{8b}$$

$$\mathrm{y} \geq 0.15 \tag{8c}$$

$$\mathrm{y} \geq (1.21 \times \mathrm{x}) - 0.27 \tag{8d}$$

$$\mathrm{y} \leq (1.21 \times \mathrm{x}) + 0.27 \tag{8e}$$

Criterion 8a enforces that the slope of the the MIR is positively increasing, and this excludes most normal star-forming galaxies that would have a dip in this region. Criteria 8b and 8c exclude objects that have bluer MIR colors, these would include non-galaxy objects like stars or passive galaxies whose only emission comes from starlight which is not emitted in the MIR (Lacy et al., 2004). Criteria 8d and 8e enforce that AGN are only selected from objects that have both red 5.8μm $-$ 3.6μm and 8.0μm $-$ 4.5μm colors.

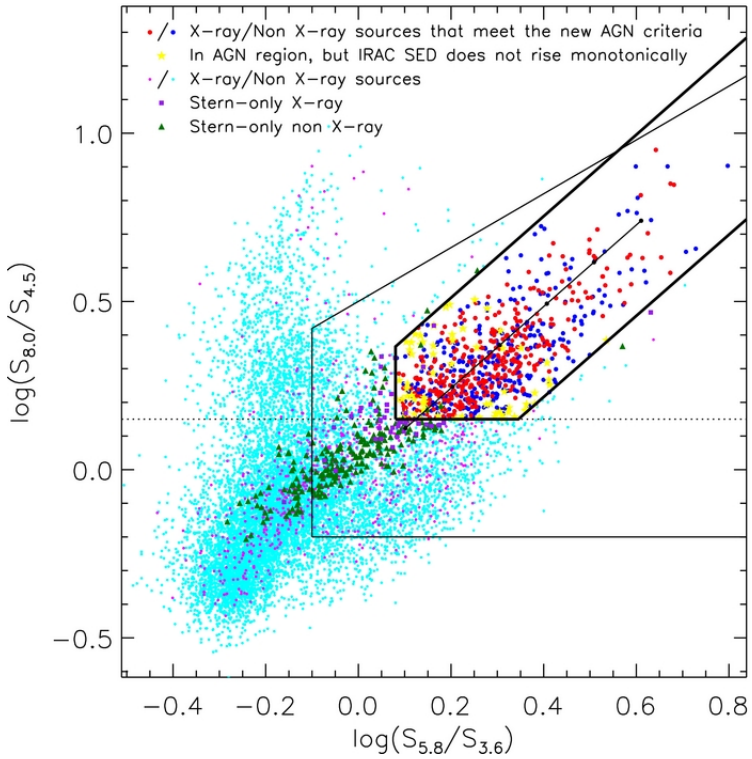

Figure 8: In IRAC color-color space, the revised Donley et al. (2012) selection criteria establishes a selection wedge outlined in the thick black line. The thin black boundary is the selection criteria from Lacy et al. (2004); Lacy et al. (2007). The small points represent sources that do not fall within the Donley et al. (2012) selection wedge. The green points represent sources that were positively identified as an AGN with a different selection schema, Stern et al. (2005). The red (dark blue) points represent X-ray (non X-ray) sources classified with this approach as an AGN. The yellow points represent sources that do fall within the selection wedge, but do that have their IRAC bands increasing monotonically (see constraint 8a). Figure credit: Donley et al. (2012).

1.6.3 Rest-Frame Emission Line AGN Detection

AGN can be detected by searching for emission lines from either of the photoionized regions (the BLR or NLR). Spectra that have broadened emission lines can conclusively be classified as an AGN, as there are no other known phenomenon that would cause the broadening (at least 3,000 km/s). (Peterson, 2006). The downside with detecting AGN by looking for broadened spectral features is

that evidence of the BLR is only present in spectra of AGN that were viewed at an angle where the dusty torus was not obscuring the view of the BLR.

Another way to detect AGN is to search for gas from the NLRs that is photoionized by AGN. Outside of the torus, the NLR emits more radially uniform than the BLR, radiating photons produced by discrete energy level transitions in atoms (Juneau et al., 2011). AGN can be detected by studying the resultant emission lines in spectra. Combinations of emission lines can be used to identify the main excitation mechanism in a galaxy. We can consider two types of excitation mechanisms: photoionization from young stars or photoionization from a power-law continuum source (Baldwin et al., 1981). Identifying the dominant excitation mechanism as the first case, photoionization from young stars, means that the source can most likely be classified as a star-forming galaxy. Sources with photonionization from a power-law continuum would include AGN. The seminal paper by Baldwin et al. 1981 uses emission line diagnostics to identify AGN by separating out sources based on their excitation mechanism. The authors identified four lines (Hα, [NII]$_{\lambda6584}$, Hβ, [OIII]$_{\lambda5007}$), to construct two line ratios ([NII]$_{\lambda6583}$/Hα, [OIII]$_{\lambda5007}$/Hβ) to use to distingush between star-forming galaxies (with an excitation source of photoionizing young stars) or AGN (with an excitation source of photoionization by continuum emission). This classification scheme is referred to as the "Baldwin, Phillips & Terlevich" (BPT) diagram. These two emission lines ratios are useful because the specific emission lines included are differently sensitive to properties star-forming and AGN galaxies. AGN have hard ionizing radiation fields from their accretion disks, which easily ionize the forbidden lines [OIII]$_{\lambda5007}$ and [NII]$_{\lambda6584}$ (Dickey et al., 2019) . This means that both ratios are larger for AGN, since [OIII]$_{\lambda5007}$ and [NII]$_{\lambda6584}$ are in the numerators. Star-forming galaxies do not have as large values for both ratios. They can take a large range of values for [OIII]$_{\lambda5007}$/Hβ, and a smaller range (with smaller values than AGN) for [NII]$_{\lambda6583}$/Hα. The diversity in values for [NII]$_{\lambda6583}$/Hα is a result of the diversity in metallicities for star-forming galaxies, as this parameter is a diagnostic for metallicity (how metal-rich a galaxy is).

Later refinements of this diagram that are commonly used included placing demarcation lines to split the parameter space into three regions: for star-forming, AGN and composite-like sources that were "in-between." Separating AGN from composite sources is the maximum starburst line from

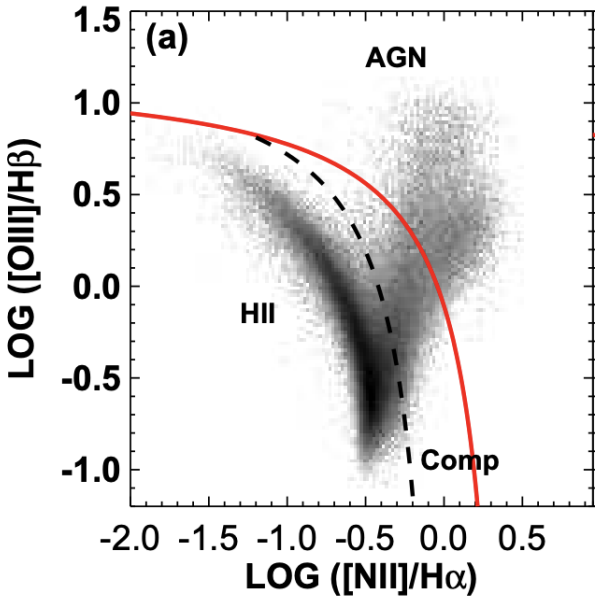

Figure 9: A BPT diagram for ∼85,000 emission-line galaxies from SDSS. The red solid line is the Kewley et al. (2001) line and is the theoretically-derived maximum starburst line. The black dashed line is the Kauffmann et al. (2003) line, which is a recalibration on the Kewley et al. (2001) based on observational data. The three separated regions are labeled. Figure credit: Kewley et al. (2006).

Kewley et al. (2001). This line was derived from modeling the locations of theoretical starburst galaxies and AGN on a BPT diagram. Separating star-forming from composite sources is the boundary from Kauffmann et al. (2003), which was an adjustment to the Kewley et al. (2001) based on empirical results which found some AGN sources lie below the maximum starburst line. Figure 19 shows an example BPT diagram for ∼85,000 emission-line sources from SDSS, and includes both the Kewley et al. (2001) (solid red) and Kauffmann et al. (2003) (black dashed) lines.

While the BPT classification scheme has proven to be useful at separating out AGN from star-forming galaxies, the original technique requires measurements for four emission lines that spans 1720Å in wavelength space. Having all four lines present in a single spectrum of a source with all four having measureable fluxes is not always possible, especially for galaxies with higher redshifts. One of the necessary lines, Hα shifts out of the observed optical range first, at $z = 0.4$. As an alternative to the BPT scheme, there is another emission line classification approach that only

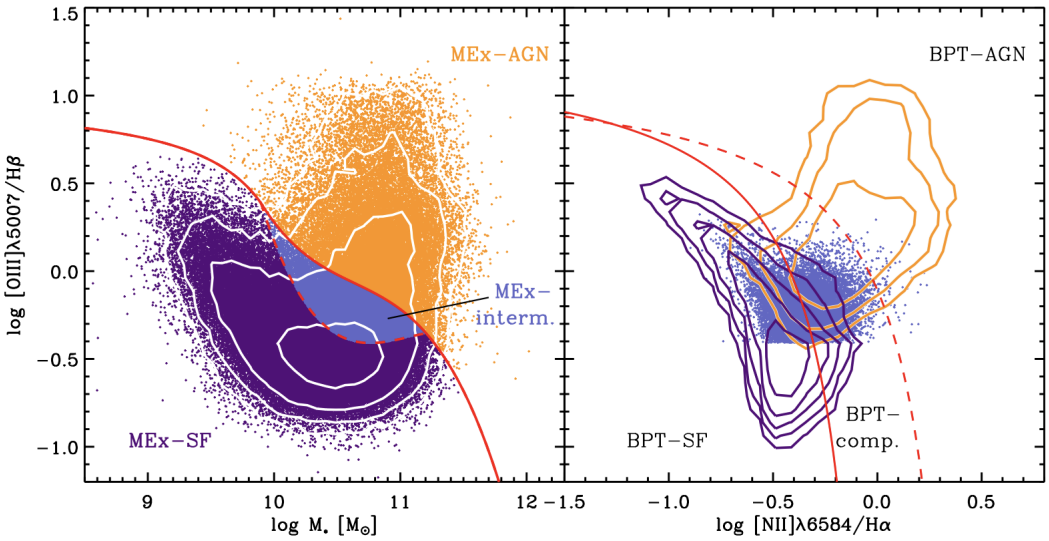

Figure 10: Left panel: A MeX diagram for SDSS sources. Sources classified as star-forming are colored purple, AGN sources are colored orange, and intermediate (composite) sources are colored blue. Right panel: A BPT diagram for the same sources as the left panel. The coloring is the same, with contours just for the star-forming and AGN classifications. Figure credit: Juneau et al. (2011).

requires two of the four emission lines. The Mass Excitation Diagram (MeX; Juneau et al. (2011)) uses $[\mathrm{OIII}]_{\lambda 5007}/\mathrm{H}\beta$ as one parameter and stellar mass as the other. The demarcation lines for the MeX were calibrated using a sample of $\sim$ 100,000 SDSS emission-line galaxies. For this classification scheme, stellar mass stands in as a proxy for $[\mathrm{NII}]_{\lambda 6583}/\mathrm{H}\alpha$ calibrated by way of the mass-metallicity relation. As previously mentioned, $[\mathrm{NII}]_{\lambda 6583}/\mathrm{H}\alpha$ is an indicator for the metallicity of a galaxy and there is a known relationship between the mass and metallicity of a galaxy (e.g., Tremonti et al. 2004; Mannucci et al. 2010). This means a classification scheme can work with the stellar mass in place of $[\mathrm{NII}]_{\lambda 6583}/\mathrm{H}\alpha$. The left panel of Figure 10 shows an example MeX diagram, that can be compared with the BPT diagram in the right panel of Figure 10 for the same sources. As show in the figure, some of the sources that the MeX classifies as "intermediate" are classified as composite in the classic BPT diagram and some of them are classified as star-forming. And some of the star-forming galaxies as classified with the MeX diagram fall into the composite range of the BPT diagram. The MeX does not have perfect correspondence the the classifications from a

BPT diagram, but it is a useful tool in cases where not all four emission lines necessary for a BPT diagram are present. The MeX diagram can be constructed for galaxies of redshifts up $z = 1$.

1.7 Motivation for Present Work

Spectroscopic analysis of galaxies has become an increasingly important way to investigate the evolution of galaxies. In the past, spectroscopic data were not as useful for large scale surveys because the process of making thousands of observations was not practical with existing technologies. In the past ∼20 years however, the usage of spectroscopy has greatly increased with the growth of facilities with multi-object spectrographs (MOS). A MOS allows for dozens to hundreds of source to have spectra observed of them at once. As explained previously, spectroscopic data are very important for their unmatched accuracy for deriving distances, mapping field densities, and recording emission lines to study. Having spectroscopic data for large numbers of galaxies in surveys can increase the utility of photometric data. For example, having a precise distance measurement from a spectroscopic redshift to use in analysis of photometric data can improve the accuracy of results.

One large survey covering approximately 800 arcmin^2 is the The Cosmic Assembly Near-infrared Deep Extragalactic Legacy Survey (CANDELS; PIs S. Faber and H Ferguson), which includes five fields that all have multi-wavelength coverage. The two GOODS fields already had highly complete spectroscopic coverage (>70%). COSMOS and UDS, however, were lacking in spectroscopic coverage. For this thesis, we reduced spectroscopic data for those two deficient fields, and we measured their redshifts and analyzed any present emisssion lines. Specifically, we measured their spectroscopic redshifts and compared them to pre-existing photometric redshifts, calculated SFRs using the emission lines, Hα and [OII]$_{\lambda 3727}$, and present sets of emission line diagnostics to detect AGN in our samples, comparing our results to other AGN detection techniques. This thesis is organized as follows: Section 2 introduces the data and observations used, as well as the selected targets included in the analysis. Section 3 describes the data reduction process, Section 4 describes the analysis of the data, including the measurements made of spectroscopic redshifts and emission line fluxes, and Section 5 discusses the results, which are summarized in the conclusion, Section 6. In this thesis, we use a standard ΛCDM cosmology with H_0= 70 km s^{-1} Mpc^{-1}, $\Omega_\Lambda = 0.7$, $\Omega_m = 0.3$

and we use a Chabrier IMF. All magnitudes are in the AB system.

2 Data and Observations

Galaxies were observed in two of the CANDELS Fields (PIs: S. Faber and H Ferguson; Grogin et al. 2011; Koekemoer et al. 2011). CANDELS is a Multi-Cycle *Hubble Space Telescope* (HST) Treasury program that obtained observations of five deep fields: the Great Observatory Origins Deep Survey (GOODS; Giavalisco et al. 2004), the North field (GOODS-N) and the South field (GOODS-S), portions of the Extended Groth Strip (EGS; Davis et al. 2007), the Cosmic Evolution Survey (COSMOS; Scoville et al. 2007), and the UKIDSS Ultra-Deep Survey (UDS; Lawrence et al. 2007; Cirasuolo et al. 2007). CANDELS was designed to focus on important time periods of the Universe, "Cosmic Dawn," when the earliest galaxies were forming just one billion years after the Big Bang, and "Cosmic Noon," around 2-3 billion years after the Big Bang when galaxies were undergoing rapid evolution and star formation. CANDELS was originally observed with the ACS optical, WFC3-IR and WFC3-UVIS instruments on the HST over 902 orbits, making it the longest HST project (Grogin et al., 2011). The five fields targeted by CANDELS all had multiwavelength coverage, and have continued to be observed in different filters, from the X-ray to Radio. The CANDELS fields are unique and unmatched in their multiwavelength photometric coverage, which makes them ideal laboratories for studying the evolution of galaxies.

2.1 CANDELS Observations and Derived Data

We used the CANDELS catalogs produced by Nayyeri et al. (2017) for the COSMOS (COS) field and by Galametz et al. (2013) for the UDS field which have observed-frame multiwavelength photometric coverage from the UV to NIR. All five fields have HST coverage with the HST/Wide Field Camera 3 (WFC3) using F160W and F125W and the HST/Advanced Camera for Surveys (ACS) using F814W and F606W. In addition to photometry from HST, we also used photometry from the Canadian France Hawaiian Telescope (CFHT), the Suprime-Cam Instrument on the Subaru Telescope (Miyazaki et al., 2002), the VIRCAM instrument on the Visible and Infrared

Survey Telescope for Astronomy (VISTA; Sutherland et al. 2015), the NEWFIRM Instrument on the Mayall telescope (Autry et al., 2003), the WFCAM instrument on the United Kingdom Infrared Telescope (UKIRT; Casali et al. 2007). We also used NIR and MIR data from the *Spitzer Space Telescope* (*Spitzer*, Werner et al. 2004), we used data from the four Infrared Array Camera (IRAC; Fazio et al. 2004) channels (3.6 μm, 4.5 μm, 5.8 μm, 8.0 μm). We used existing IRAC data for both fields. For COSMOS, we used data from a few IR surveys of the field: the COSMOS Spitzer Survey (S-COSMOS; Sanders et al. 2007), and from the Spitzer Extended Deep Survey (SEDS, Ashby et al. 2013), which was coupled in the COSMOS2015 catalogue (Laigle et al., 2016), along with smaller programs targeting the COSMOS field with *Spitzer*. For the UDS field, we used IRAC data from the SEDS survey as well, and additionally, from the *Spitzer*-CANDELS (S-CANDELS, Ashby et al. 2013) program. Data from the IRAC instrument was also used to identify AGN, as discussed in Section 5.3. A summary of the filters used from these various instruments is given in Table 1 for COSMOS and Table 2 for UDS.

The source catalog for the CANDELS field was generated using the detection algorithm `SExtractor` (Bertin & Arnouts, 1996) which was applied to the F160W (H-band) CANDELS mosaics. `SExtractor` uses the input image to define the boundaries of each galaxy, setting the constraining area for the photometry to be integrated over for each galaxy. The photometry was matched to a consistent spatial resolution using the TFIT algorithm (Laidler et al., 2007). In addition to the photometric data, these catalogs also include photometric redshifts, prepared as described in Dahlen et al. (2013). The photometric redshifts used are the median results for photometric redshifts estimated using eleven different SED fitting codes and template libraries. In a test sample using galaxies from the CANDELS GOODS-S field, combining the results of multiple SED fitting setups by taking a median resulted in less scatter and fewer outliers when computing photometric redshifts (Dahlen et al., 2013).

Stellar masses were also included in these catalogs. Ten different groups from the CANDELS team fit the SEDs constructed from available CANDELS data using the same set of templates but different choices for fitting codes, physical assumptions, and parameters. For each galaxy, the stellar mass included in the catalog is the median of the ten stellar masses for that galaxy (Mobasher et al.,

Instrument	Filter	$\lambda_{\rm eff}$[Å]	5σ depth ($\rm mag_{AB}$)	Reference(s)
CFHT	u*	3817	27.31	Gwyn (2012)
	g*	4860	27.69	
	r*	6220	27.18	
	i*	7606	27.23	
	z*	8816	26.18	
Subaru / Suprime-Cam	B	4448	27.98	Taniguchi et al. (2015)
	V	5470	26.78	
HST/ACS	F606W	5919	28.34	Koekemoer et al. (2011)
	F814W	8060	27.72	
HST/WFC3	F160W	15369	27.56	Koekemoer et al. (2011)
VISTA / VIRCAM	Y	10210	25.47	McCracken et al. (2012)
	J	12524	25.26	
	H	16431	24.87	
	K_s	21521	24.83	
Mayall / NEWFIRM	J_1	10460	24.60	Whitaker et al. (2011)
	J_2	11946	24.32	
	J_3	12778	24.26	
	H_1	15601	23.86	
	H_2	17064	23.45	
	K	21700	23.80	
Spitzer / IRAC	3.6μm	35569	24.41	Sanders et al. (2007); Laigle et al. (2016)
	4.5μm	45020	24.4	
	5.8μm	57450	21.28	
	8.0μm	79158	21.2	

Table 1: Photometric data used from the COSMOS CANDELS catalog. The 5σ limiting depths come from Nayyeri et al. (2017).

2015; Santini et al., 2015). For the initial target selections, we used these stellar masses from the CANDELS catalogs. However, for the analysis in this thesis, we obtained new stellar masses and star formation rates from SED fitting with the code `MAGPHYS` (da Cunha et al., 2011). The complete process for this is described in Section 4.3. We derived new stellar masses and SFRs using `MAGPHYS` because the original properties included in the CANDELS catalogs were from SED fitting that did not have the precise spectroscopic redshifts available that we did for our analysis. As described in Section 1.2, spectroscopic redshifts are superior to photometric redshifts because they are more precise.

Instrument	Filter	$\lambda_{\rm eff}$[Å]	5σ depth ($\rm mag_{AB}$)	Reference(s)
CFHT / MegaPrime	u*	3817	27.68	Almaini et al., in prep
Subaru / Suprime-Cam	B	4448	28.38	Furusawa et al. (2008)
	V	5470	28.01	
	$\rm R_c$	6276	27.78	
	i'	7671	27.69	
	z'	9096	26.67	
HST / ACS	F606W	5919	28.49	Koekemoer et al. (2011)
	F814W	8060	28.53	
HST / WFC3	F160W	15369	27.45	Koekemoer et al. (2011)
UKIRT / WFCAM	J	1251	25.63	Almaini et al., in prep
	H	1636	24.76	
	K	2206	25.39	
Spitzer / IRAC	3.6μm	35569	24.72	Ashby et al. (2013,?)
	4.5μm	45020	24.61	
	5.8μm	57450	22.30	
	8.0μm	79158	22.26	

Table 2: Photometric data used from the UDS CANDELS catalog. The 5σ limiting depths come from Galametz et al. (2013).

2.2 X-ray Data

We use deep X-ray data from *Chandra X-ray Observatory* as one method to identify AGN. Observations for COSMOS (Chandra COSMOS-Legacy Survey; Elvis et al. 2009; Civano et al. 2016; Marchesi et al. 2016) were taken with the full band (0.5–10 keV) limiting fluxes of 9×10^{-16} erg $\rm s^{-1}$ $\rm cm^{-2}$. The integrated exposure time for the observations was $\sim$ 4.6 Ms (for the entire COSMOS field, which is a superset of the CANDELS COSMOS field). These observations resulted in a final catalogue of 4016 sources, 97% of which had matching photometric redshifts and data (Marchesi et al., 2016).

Chandra observations for UDS came from the *Chandra* survey of the UDS field (X-UDS; Kocevski et al. 2018) and were taken with the full band (0.5–10 keV) limiting fluxes of 4.4×10^{-16} , respectively. The observations had an integrated exposure time of $\sim$ 1.25 Ms. The X-UDS survey was designed to identify a sample of obscured AGN around Cosmic Noon. The secondary goal of X-UDS was complement existing *Spitzer* observations to study the cosmic backgrounds (both IR

and X-ray) to study one of the earliest populations of supermassive black holes.

2.3 Mid- and Far-Infrared Data

We also included photometry from the mid- and far-IR. We did this to have a better constraint on the actual SFRs when fitting our SEDs. We used observations from the the Multiband Imaging Photometer for Spitzer (MIPS; Rieke et al. 2004), including both the 24 and 70 μm data for COSMOS, with 71 μJy and 7.5 mJy 5σ depth respectively from the COSMOS Spitzer survey (S-COSMOS; Sanders et al. 2007). For UDS, we used the 24 μm data with 300 μJy 15σ depth from the Spitzer UKIDSS Ultra Deep Survey (SpUDS; PI: J. Dunlop).

Additionally, we used FIR data from the *Herschel Space Observatory* (*Herschel*; Pilbratt et al. 2010), from both the Photoconductor Array Camera and Spectrometer (PACS; Poglitsch et al. (2010) using the 100 and 160 m bands, which have a 2.9 (14.4), and 6.6 (26.7) μJy 5σ limiting depth respectively for COSMOS (UDS). We also used data from the Spectral and Photometric Imaging Receiver (SPIRE; Griffin et al. 2010) 250, 350, and 500μm bands. The PACS data comes from the PACS Evolutionary Probe (PEP; Lutz et al. 2011) survey. The SPIRE obervations used in the paper came from the the *Herschel* Multitiered Extragalactic Survey (HerMES; Oliver et al. 2012), have a 5σ limiting depth of 11.0 (19.4), 9.6 (19.2) and 11.2, (20.0) mJy for the 250, 350, and 500 μm bands respectively for COS (UDS). Many of our sources were selected based on their detection with *Herschel* for being extra luminous in the infrared.

2.4 Target Selection

The galaxies in this study came from two of the CANDELS fields, COSMOS and UDS. For this project, we reduced and analyzed multi-object spectroscopy of sources in these fields from the Gemini Multi-Object Spectrographs (GMOS) on the twin Gemini-North and Gemini-South Telescopes (Hook et al., 2004; Gimeno et al., 2016). The sample presented in this thesis represents a compilation of galaxies from three GMOS observing programs: two for the CANDELS COSMOS field ("COS"), one on Gemini-N and the other on Gemini-S (GMOS IDs: GN-2014A-Q-10, GS-2019A-Q-219), and one for UDS on Gemini-S (GS-2014B-Q-23+GS-2016B-Q-18). A summary of

the programs is given in Table 3.

The 2014 Gemimi-N and the 2016 Gemini-S observations, ("GMOS-N COS" and "GMOS-S UDS") were designed to address a lack of spectroscopic coverage of star-forming *Herschel*-selected galaxies in the COSMOS and UDS fields. The *Herschel Space Observatory* is an infrared (IR) space observatory that is sensitive to the energy of star-forming galaxies which prevails in the far-IR regime. *Herschel* does not have very high sensitivity, so it only detects the brightest FIR sources. For surveys like CANDELS that have been observed with *Herschel*, sources that are actually detected are very strong emitters in the FIR, and thus, must be actively undergoing star formation at high rates to create the FIR emission (see Section 1.5.2). These *Herschel* selected galaxies are called luminous or ultraluminous infrared galaxies (LIRGs, $L_{IR} > 10^{11} L_{\odot}$ and ULIRGs, $L_{IR} > 10^{12} L_{\odot}$), which are galaxies that are strongly emitting in the infrared, as a consequence of enhanced rates of ongoing star formation (Sanders & Mirabel, 1996). Many of these galaxies are expected to be involved in a merger event with another galaxy (Kartaltepe et al., 2010). Obtaining spectroscopy of (U)LIRGs in the COSMOS and UDS CANDELS fields will complement the existing multi-wavelength photometric coverage, including the *Herschel* data already observed. The accuracy of properties derived from the existing photometric data through SED fitting is depdendent on the accuracy of the measured redshift, with spectroscopic redshifts being the most accurate. Additionally, spectroscopic data is necessary to study the the effects of environment and density on galaxies. While the two GOODS fields have high spectroscopic completeness, the fields themselves are small in size, limiting the full range of environment densities that can studied. Obtaining spectroscopic redshifts for larger CANDELS fields such as COSMOS and UDS will aid in our ability to study the

Program Name	Program ID(s)	Years Obs.	Targeted Sources
GMOS-N COS	GN-2014A-Q-10	2014	*Herschel*-selected (U)LIRGs
GMOS-S UDS	GS-2014B-Q-23,	2014,	*Herschel*-selected (U)LIRGs
–	GS-2016B-Q-18	2016	–
GMOS-S COS	GS-2019A-Q-219	2019	Close-pair candidates

Table 3: A summary of the programs used in this thesis, including the names used to reference them, their associated Gemini program ID(s), the years they were observed, and the types of sources they targeted.

effects of environmental density on galaxies and their properties.

The third program ("GMOS-S COS") was designed to obtain spectroscopy for close-pair merger candidates in the COSMOS field. These data would be used in conjunction with other archival spectroscopy to buld a large sample of spectroscopically confirmed galaxy pairs out to $z \sim 1.5$ with separations from 1-150 kpc. Close-pairs are galaxies with a very small projected separation, and which are assumed to be in the early stages of a merger. These close-pair candidates came from a parent sample of CANDELS galaxies that had projected separations 5-150 kpc based on pre-existing photometric redshifts. These sources are important to study because mergers are expected to affect the evolution of galaxies, so studying galaxies at all stages of mergers is important (Shah et al., 2020). All three programs targeted objects for their respective science goals, but also included filler targets, which were sources in the fields without existing spectroscopic redshifts but with known photometric redshifts of $0.7 \leq z_{\rm phot} \leq 1.5$ with an i-band magnitude of $I_{AB} < 24$. Filler targets were included to maximize the observing time when there was extra room in the mask designs after fitting in the targets.

2.5 GMOS Observing Strategy

The GMOS instruments have a $5.5' \times 5.5'$ square view. Both the CANDELS COSMOS and UDS fields subtend an area approximately $9' \times 15'$. For the 2014 GMOS-S observations of UDS and the 2016 GMOS-N observations of COSMOS, each field of interest was covered in its entirety with a spread of 8 pointings. We used 16 masks (5.5' squares) to cover the 8 pointings using two passes, in order to maximize the number of objects that could be observed. The positioning of some masks was shifted for the second pass in order to capture objects on the edge of the field. For the 2016 GMOS-S UDS observations mask 16 was not observed, and for GMOS-S COS, only six of the eight masks were ever observed. The mask configurations are shown in Figure 11.

Each mask was observed with two different central wavelengths (either 720Å and 725Å or 820Å and 825Å). The purpose of using two central wavelengths was to ensure that the chip gaps would be covered and there would be a continuous spectrum. All of the observations involved operating the GMOS instrument in "nod and shuffle" mode, which makes use of a CCD's ability to store two

images of a field that were observed quasi-simultaneously. The instrument is shifted at the same time charge is transferred, so images of the sky and the target source can be taken on the same optical paths and read out only once. During these observations, the telescope "nods" between the sky and target, storing the spectra of the component not being visualized on the un-illuminated parts of the CCD. The observations were taken in this mode to ensure the best results for sky subtraction during later processing at longer wavelengths.

Our programs were all done in queue mode, which meant that Gemini scientific staff actually carried out the observations according to our proposed specifications. A summary of the observations, including dates observed, exposure times, number of slits per mask and weather during observations is shown in Table 4.

	Program ID	Mask	Slits Obs.	Slits Det.	Dates Obs.	Total Exp. (s)	Weather Comments
GMOS-N COS	GN-2014A-Q-10	1	26	9	2014-05-03	6120	Photometric conditions
	GN-2014A-Q-10	2	26	4	2014-05-04	6120	Photometric conditions
	GN-2014A-Q-10	3	28	10	2014-12-16	6120	No data available
	GN-2014A-Q-10	4	27	4	2014-12-22	6120	Photometric conditions
	GN-2014A-Q-10	5	27	6	2014-12-29	6120	Photometric conditions
	GN-2014A-Q-10	6	28	7	2014-12-30	5160	Photometric conditions
	GN-2014A-Q-10	7	26	10	2015-01-14	6120	Photometric conditions
	GN-2014A-Q-10	8	27	11	2015-01-15	6120	Poor conditions
	GN-2014A-Q-10	9	25	10	2015-01-21	6120	Poor conditions
	GN-2014A-Q-10	10	27	10	2015-01-22	6120	Poor conditions
	GN-2014A-Q-10	11	26	9	2015-01-22	6120	Poor conditions
	GN-2014A-Q-10	12	26	6	2015-01-24	6120	Poor conditions
	GN-2014A-Q-10	13	26	9	2015-01-26	5160	Photometric conditions
					2014-01-27	960	Poor conditions
	GN-2014A-Q-10	14	27	8	2015-01-27	6120	Poor conditions
	GN-2014A-Q-10	15	29	8	2015-01-25	6120	Photometric conditions
	GN-2014A-Q-10	16	27	2	2015-01-27	6120	Poor conditions
GMOS-S COS	GS-2019A-Q-219	1	27	3	2019-02-25	5808	–
					2019-03-04	5808	–
	GS-2019A-Q-219	2	27	11	2019-03-05	7744	–
					2019-03-06	1936	–
					2019-03-15	1936	–
	GS-2019A-Q-219	4	25	4	2019-04-01	5808	–
					2019-04-03	5808	–
	GS-2019A-Q-219	5	21	3	2019-03-17	5808	Mostly clear skies
					2019-03-20	5808	–
	GS-2019A-Q-219	7	29	5	2019-04-09	5808	–
	GS-2019A-Q-219	8	25	3	2019-03-15	968	–
					2019-03-16	2904	–
					2019-03-17	2904	Mostly clear skies
					2019-03-23	4840	–
GMOS-S UDS	GS-2016B-Q-18	1	27	8	2016-10-06	2904	–
					2016-10-09	3267	–
	GS-2014B-Q-23	2	26	5	2015-01-20	968	–
					2015-01-23	1936	–
					2015-12-05	3267	Seeing stable
	GS-2014B-Q-23	3	26	6	2015-12-09	2904	–
					2015-12-15	3267	–
	GS-2014B-Q-23	4	26	7	2015-12-16	3267	–
					2016-01-13	2904	–
	GS-2014B-Q-23	5	28	10	2014-11-27	6171	–
	GS-2014B-Q-23	6	24	5	2016-01-01	2178	–
					2016-01-15	1089	–
					2016-02-03	2904	–
	GS-2016B-Q-18	7	26	7	2016-10-06	3267	–
					2016-10-08	2904	–
	GS-2016B-Q-18	8	27	4	2016-11-02	3267	–
					2016-12-05	2904	Conditions clear
	GS-2016B-Q-18	9	25	3	2016-12-02	6171	–
	GS-2016B-Q-18	10	26	8	2016-12-24	3267	–
					2017-10-14	2904	–
	GS-2016B-Q-18	11	26	3	2016-12-04	3267	Conditions clear
					2016-12-05	2904	Conditions clear
	GS-2016B-Q-18	12	26	3	2017-10-14	2904	–
					2017-10-22	3267	–
	GS-2016B-Q-18	13	29	5	2017-10-25	6171	Non-photometric
	GS-2016B-Q-18	14	28	2	2017-10-26	6171	Thin, rolling clouds
	GS-2016B-Q-18	15	26	5	2017-11-18	3267	–
					2017-12-21	2904	–

Table 4: Observation summaries for the three programs, showing the program IDs, the number of slits observed, and the number of slits with actual detections, the dates of observations, the exposure time and the weather at the time of each observation. Weather comments came from the observing logs where possible. For GMOS-N observations without weather comments, we record the conditions from the SkyProbe instrument on the Canadian French Hawaii Telescope which is also on Mauna Kea where GMOS-N is.

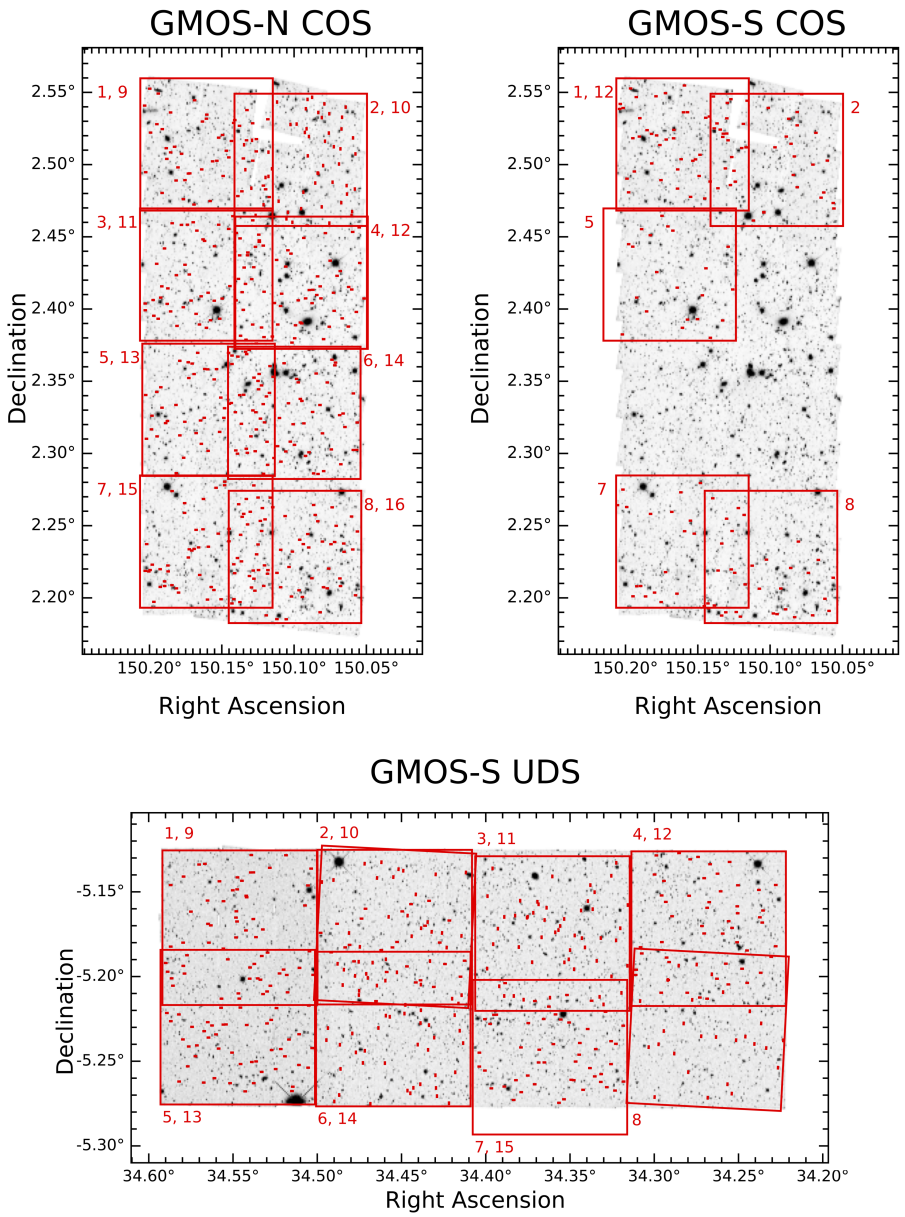

Figure 11: The mask designs overlaid (red) on an F160W HST mosaic are shown for the three different observing programs. Note that we only show here the masks that were actually observed, and not just planned. Starting from the upper plot left and going clockwise, the corresponding GMOS program IDs are: GN-2014A-Q-10, GS-2019A-Q-219, GS-2014B-Q-23+GS-2016B-Q-18.

3 Data Reduction and Processing

3.1 Reduction Pipeline

We reduced the GMOS observations with an automated process we developed that uses tasks from the IRAF Gemini package version 1.14 (Gemini Observatory & AURA, 2016). The data products from the GMOS instruments are stored in multi-extension fits (MEF) files, with each extension of the science files corresponding to an individual slit in the mask. The framework of the reduction process was to first process the associated calibration files (i.e., the bias files, the flats, and the arcs) and then to apply those calibrations to the science files. First, a Masterbias file was created with bias fields taken within one month of the science observations. Masterflats were created using the task `gsflat` which combines the individual flats and removes the GCAL (the facility calibration unit) spectral response.

The spectra were wavelength calibrated using the arc calibration files, which are spectra of of a CuAr lamp taken on the date of observations. To prepare for this step, the science files and arc files were both reduced using the `gsreduce` task, which invokes a call to several tasks that trim the overscan region, apply the flat field correction and mosaic the extensions. The mosaic-ing step involved stitching together the n $\times$ m different extensions that come from the observation arrays being read out through n amplifiers across m CCD chips. For our 2016 and 2019 GMOS-S observations, there were 12 extensions of each file, as are 3 chips readout through 4 amplifiers in the Hamamatsu arrays. For the 2016 GMOS-N observations, there are only 6 extensions per file (3 chips and 2 amplifiers per chip) as this was prior to the upgrade of the detector.

The wavelength solution usually could be performed automatically, however if a single science slit fails, all slits needed to be interactively fit. After the wavelength solution was applied, we combined the two offset wavelengths of each observation, being considerate of the fact they were taken in Nod and Shuffle Mode. For the GMOS-N observations, it was necessary for us to supply the DTA offset which indicates shift of the spectral image. The offset was set so as to suppress the linear charge traps that affected Nod and Shuffle observations. This was not necessary for the GMOS-S observations, as DTA offsetting is not necessary with the upgraded Hamamatsu detectors.

Our output data product for each object was a MEF for each mask, where each extension of a single MEF is the reduced two-dimensional spectrum of a slit. For our science purposes, we needed to extract along each two-dimensional spectrum to get a one-dimensional spectrum. To do this, we manually identified the correct y-position to extract along by looking for the presence of emission lines in the two-dimensional spectrum and extracted a horizontal slice with a three pixel extraction aperature. Auto extraction was not an option for our data set as these targets are quite faint. The ratio of 1D spectra we were able to extract to the number of targets observed was 135/428 for GMOS-N COS, 29/154 for GMOS-S COS, and 78/396 for GMOS-S UDS.

An example of a reduced 2d-spectrum and its respective 1d-spectrum is shown in Figure 12. The spectrum has been put into rest-frame using the redshift measured as described in Section 4.1. The flux units in the 1d spectrum are in physical flux density values, determined using the flux calibration procedure in Section 3.2.

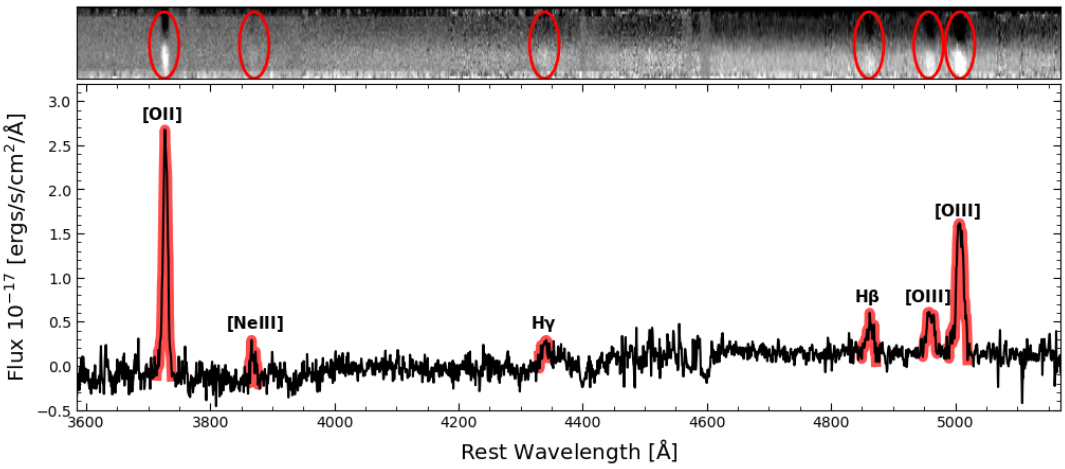

Figure 12: An example rest-frame spectrum for one galaxy, COSMOSJ100043.54+022524.27, with a measured spectroscopic redshift of $z = 0.7281$. The upper panel shows the reduced two-dimensional spectrum and the lower panel shows the extracted one-dimensional spectrum. The one-dimensional spectrum has been continuum subtracted and flux-calibrated as described in Section 3.2. Six emission lines are visible in both the one- and two-dimensional spectrum and were identified with the emission line fitting software `ALFA` (see Section 4.2). From increasing wavelength, the present emission lines are $[\mathrm{OII}]_{3726,3729}$, $[\mathrm{NeIII}]_{3869}$, Hγ, Hβ, $[\mathrm{OIII}]_{4959}$, and $[\mathrm{OIII}]_{5007}$. The [OII] doublet is not resolved in this example.

3.2 Flux Calibration Technique

To flux calibrate our spectra, we took a two-pronged approach. The first correction we applied was to the overall shape of the spectrum, and that correction came from the sensitivity function of a standard star observed with the same instrument as the science observations. The sensitivity functions were produced using tasks from the Gemini package of IRAF. At the same time that we applied the sensitivity function to each spectrum, we also performed an extinction correction using the observatory's extinction curve.

The second step to our flux calibration was to perform a spectrophotometric calibration. For each mask, we picked a slit that has visible continuum. We then estimated what flux would be measured by the HST ACS F814W filter, by taking the product of the spectrum and filter transmission curve integrated over wavelength and normalized by the integral of the transmission curve over wavelength. This is expressed mathematically as,

$$F_\lambda = \frac{\int f_\lambda \times T_\lambda \, d\lambda}{\int T_\lambda \, d\lambda}, \tag{9}$$

where F_λ is the flux through the filter, f_λ is the spectrum's flux, and T_λ is the transmission curve.

The object in the slit chosen must have a photometric flux value for F814W. For galaxies lacking that value, we substituted the SuprimeCam i-band photometric flux and filter from the Subaru telescope (Miyazaki et al., 2002). These values came from the CANDELS photometric catalog described in Section 2.2. By comparing the measured photometric flux value to the estimated flux from the convolution technique, we were able to calculate a scaling ratio to apply to all of the spectra in the mask, which converted the flux of the spectra from instrumental units to the physical flux density units of erg/s/cm^2/Å.

4 Analysis

4.1 Measuring Redshifts

We measured spectroscopic redshifts using SpecPro (Masters & Capak, 2011), an interactive IDL program for measuring redshifts. The input for SpecPro includes three files per source: the one dimensional spectrum, the two dimensional spectrum, and an info file that includes the coordinates and additional desired information, such as a pre-existing photometric redshift. Within the SpecPro interface, emission line markers can be overlaid and shifted left and right, until a match is found and the corresponding redshift is recorded. In cases where there was only one obvious feature, the pre-existing photometric redshift was used to help guide the judgement of the user.

Quality Flag	Description
4	Solid: Two or more strong features; 98% confident
3	Good: One strong and one weak feature; 95% confident
2	Fair: Weak feature or single emission line that cannot be distinguished; 75% confident
1	Dubious: Based on potential or weak feature; 50% confident
-2	Bad data quality, no redshift measurable

Table 5: Quality Flag Descriptions.

A quality flag for each measurement was assigned, based on a scale of one to four, with four being the highest certainty (see Table 5). We measured redshifts, and compared with an independent measurement by a second person (Dr. Ekta Shah), and then the consensus redshift and quality flag were recorded for each source. For the majority of cases, the two individuals examining the redshifts were in agreement prior to discussion, and in all cases were able to reconcile differences after meeting. For GMOS-N COSMOS, out of 428 targeted 1d spectra, 124 had measured redshifts (of any quality flag), for GMOS-S UDS the ratio was 64/396, and for GMOS-S COSMOS, the ratio was 8/154.

The distribution of redshifts broken down by quality flag is shown graphically in Figure 13.

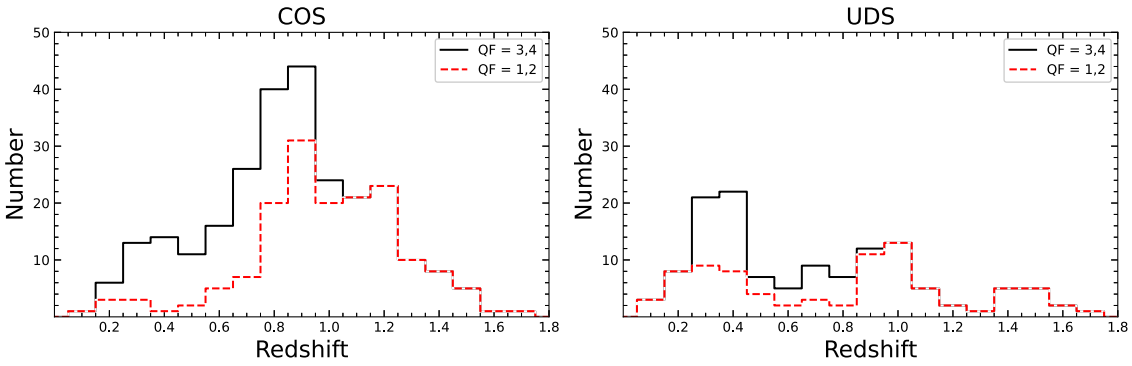

Figure 13: The stacked distributions of measured redshifts for COS (left panel) and UDS (right panel). The height of the area upper-bounded by black represents the number of high QF sources at each redshift, and the height of the area upper-bounded by red represents low QF sources.

The distributions for the high-QF and low-QF sources in COS are mirrored, both peaking within $0.8 \leq z \leq 1.0$, but with the high-QF sources skewed more towards lower redshifts and the low-QF sources skewed more towards higher redshifts. All of the high-QF sources for COS are $z \leq 0.982$. For UDS, there is not as clear a distribution, which is not unexpected since there are many fewer sources. There are low-QF sources at all redshift ranges and the high-QF sources are $z \leq 0.878$.

Table 6 shows the number of redshifts with each QF for each of the three programs, separating out the two GMOS-S programs. For GMOS-S COS, 7/7 measured spectroscopic redshifts were low QF. For GMOS-S UDS, 42/64 sources were low QF. For GMOS-N COS, 64 out of 115 sources were low QF. We show the individual redshifts measured for each galaxy and its associated quality flag in Appendix A.

Field	QF = 1	QF = 2	QF = 3	QF = 4
GMOS-N COS	20	54	12	39
GMOS-S COS	6	1	0	0
GMOS-S UDS	22	20	9	13

Table 6: Quality Flag Breakdown by program.

Emission Line	N
[OII] λ3727	87
[OII] λ3729	57
[NeIII] λ3869	3
Hδ λ4102	5
Hγ λ4341	24
Hβ λ4861	75
[OIII] λ4959	44
[OIII] λ5007	71
HeI λ5876	0
[OI] λ6364	0
[NII] λ6548	10
Hα λ6563	36
[NII] λ6583	18
[SII] λ6716	18
[SII] λ6731	13

Table 7: The number of galaxies with S/N> $ss3$ detections for each emission line.

4.2 Measuring Emission Line Fluxes

After spectroscopic redshifts were measured, we put the spectra in their rest frame. To measure emission lines, we used a command line program, Automated Line Fitting Algorithm (`ALFA`; Wesson 2016). Unlike most line-fitting codes, `ALFA` utilizes a genetic algorithm to construct a synthetic spectrum based on a list of lines expected to be present. `ALFA` also has the benefit of being fully automated and able to measure lines from a single spectrum in just seconds on a standard laptop. In Table 7, we show the number of galaxies with each emission line at S/N > 3.

Figure 14 shows a graphical depiction of the number of sources with detections of different combinations of the five strong emission lines: Hα, Hβ, [NII]$_{\lambda6583}$, [OIII]$_{\lambda5007}$, and [OII]$_{\lambda3727}$. 36 sources have an Hα emission line, 75 have Hβ, 18 have [NII]$_{\lambda6583}$, 87 have [OII]$_{\lambda3727}$, and 71 have [OIII]$_{\lambda5007}$. We included these lines specifically as they were used in other parts of our analysis, for constructing optical diagnostic diagrams and also for use as SFR indicators. To construct a BPT diagram we need Hα, Hβ, [NII]$_{\lambda6583}$, and [OIII]$_{\lambda5007}$. Nine sources had all four of these lines. For SFR indicators, we used Hα and [OII]$_{\lambda3727}$, only one source had both of these lines. This is not unexpected because of the large distance in wavelengths between those two emission lines.

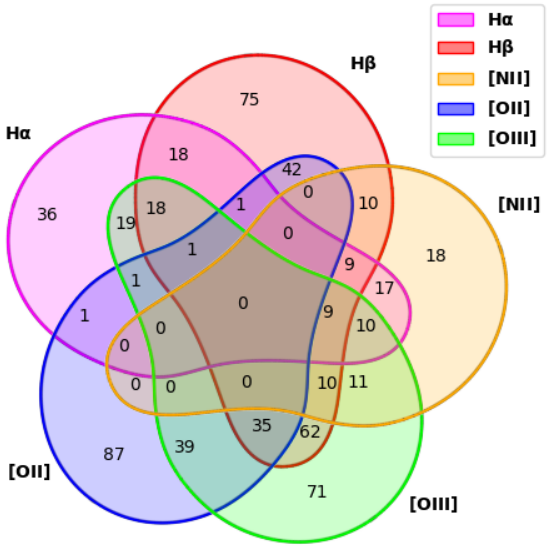

Figure 14: This Venn diagram shows the number of each sources that have a particular combination of emission lines. The number in the outer part of each bulb shape indicates how many galaxies in total that had spectra with the labeled emission line detected at S/N > 3. The number in the overlapping shape regions indicate the number of sources that have the emission lines represented by the shapes being overlapped. For example, 36 sources have an Hα emission line, 75 have Hβ, 18 have [NII]$_{\lambda 6583}$, 71 have [OIII]$_{\lambda 5007}$, and 87 have [OII]$_{\lambda 3727}$. Only nine galaxies have all four of those lines. Some regions contain a zero because there were no sources that contained all of those lines.

4.3 Flux Attenuation Corrections and SED modeling

We corrected the fluxes for the effects of attenuation to compare to the measured fluxes. In order to correct for these effects, we used a model of each galaxy's SED for both an attenuated and unattenuated fit. We used the SED fitting software `MAGPHYS` (da Cunha et al., 2011), which works by imposing an energy balance constraint between a galaxy's stellar emission and its dust content. We constructed an SED for each of our galaxies using multiwavelength photometry from the UV to the IR, including available FIR data from *Herschel* as described in Sections 2.1 and 2.4. We used the (unpublished) CB07 stellar population synthesis models. We used the outputted stellar mass and SFR from `MAGPHYS` in later analysis, as described in Sections 5.2 and 5.3.

Additionally, we used the outputs of `MAGPHYS` as a means to correct our measured fluxes for

attenuation. The output of MAGPHYS includes the best-fit model for both the attenuated and unattenuated SEDs. For the rest-frame wavelength of each emission line we measured, we computed the ratio of the SED model's attenuated to unattenuated flux and then used that value to scale our measured fluxes to correct them for attenuation from dust. The corrected flux is,

$$\mathrm{F}_{\lambda,\mathrm{corr}} = \mathrm{F}_{\lambda} \times \frac{\mathrm{f}_{\lambda}}{\mathrm{f}_{\lambda,\mathrm{atten}}}, \tag{10}$$

where $\mathrm{F}_{\lambda,\mathrm{corr}}$ is the attenuation corrected flux for a line at wavelength λ, F_{λ} is that line's uncorrected flux, f_{λ} is the un-attenuated flux at that wavelength from the MAGPHYS fit, and $\mathrm{f}_{\lambda,\mathrm{atten}}$ is the attenuated flux from MAGPHYS.

5 Results and Discussion

5.1 Redshift Comparison and Completeness

We compared our measured spectroscopic redshifts to existing photometric redshifts, as shown in Figure 15. We found a correlation between the spectroscopic and photometric redshifts with a mean dispersion of ($\langle \Delta z/(1+z) \rangle$) of 0.01927 for COSMOS and 0.01684 for the UDS sample. Note that we combined the GMOS-N COS and GMOS-S COS into the same sample. We defined outliers as ($|\Delta z/(1+z)| > 0.15$), and while there are certainly outliers visible in Figure 15, 90.9% of the outliers were low quality flags (QF = 1,2) for COSMOS and 93.3% of the outliers were low quality flags for UDS.

We posited that these outliers sources were most likely fainter galaxies. To investigate this, we plotted the fractional success rate of targets with measurable spectroscopic redshifts (out of observed targets) versus the I-band magnitude (ACS F814W). These results are binned by I-band magnitude and are shown in Figure 16. Particularly for UDS, a higher fraction of the fainter sources were associated with a low QF redshift. This explains why so many of the UDS outliers were low QF, because the low QF sources were fainter and therefore did not have as clear a spectrum. Since the GMOS-S COS sources were not also all faint, we cannot confirm that the observatory played a

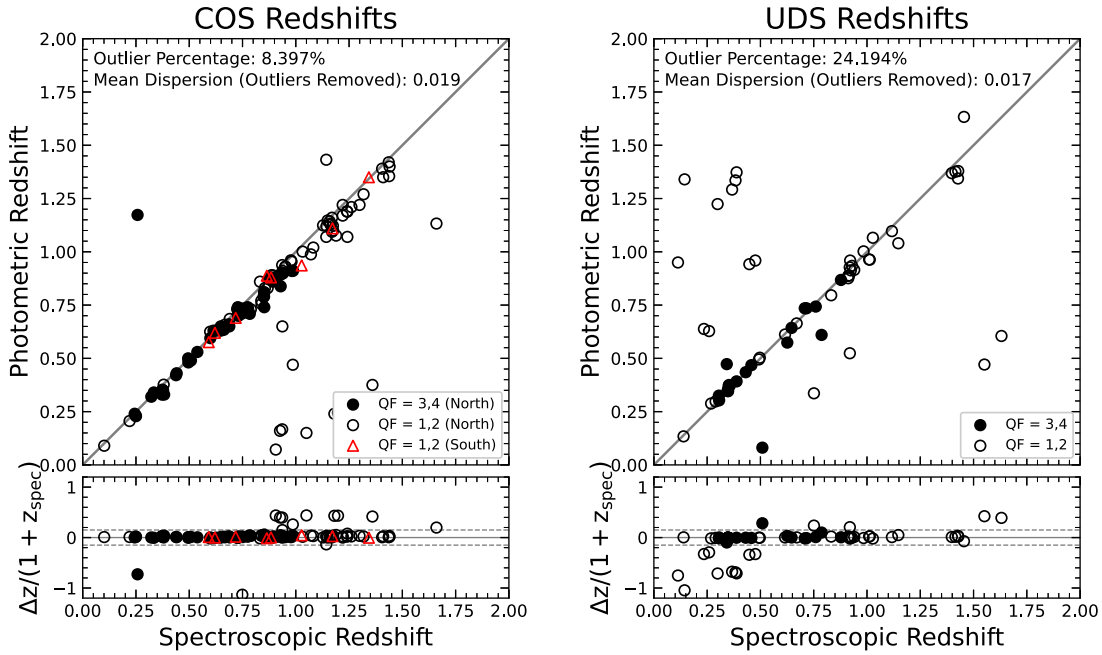

Figure 15: Upper panels: photometric redshift compared to spectroscopic redshift for the COS (left) and UDS (right) GMOS observations. The solid line represents the one-to-one line where points on that line represent sources that have the same photometric and measured spectroscopic redshift. Lower panels: the residuals between the photometric and spectroscopic redshifts, divided by $1 + z_{spec}$. Dashed lines are used to demarcate boundary lines for outliers, which are defined as $|z_{spec} - z_{phot}| / (1 + z_{spec}) > 0.15$. In both panels, sources with a low quality flag (QF = 1 or 2) are denoted by open shapes and sources with a high quality flag (QF = 3 or 4) are represented by closed shapes. For the left panel, we differentiate between sources from the 2014 run on GMOS-N and 2019 run on GMOS-S using a circle for the GMOS-N sources and a triangle for the GMOS-S sources. Note that there were no COS GMOS-S sources with a high quality flag. See Section 4.1 for a description of the quality flag system.

role in these results, however the sample size for GMOS-S COS is very small (8 objects). Another explanation for the higher outlier fraction for UDS might be that there was poorer weather during those observations. Due to the lack of weather data available (see Table 1), we cannot definitively conclude this was the case. Also of interest is comparing the outliers for each program. As shown in Table 6, a higher fraction of redshifts were low QF for GMOS-S (GMOS-S UDS + GMOS-S COS) compared to GMOS-N observations.

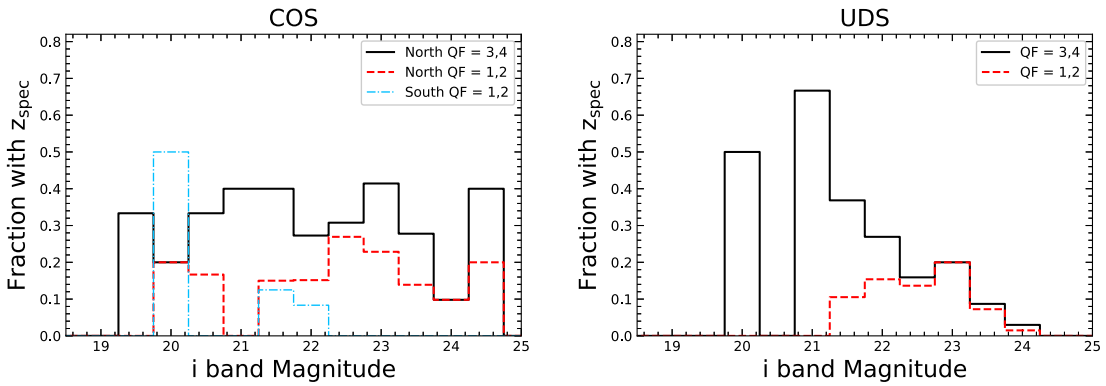

Figure 16: The fractional success rate (targets with measurable spectroscopic redshifts) are plotted for bins of I-band (F814W) magnitude for COS sources (left panel) and UDS sources (right panel). The I-band magnitudes of sources with high QF redshifts are shown in solid black and the I-band magnitude of sources with low QF redshifts are shown in dashed red. For the left panel, sources part of the two COS programs (GMOS-N COS and GMOS-S COS) are separated out, with sources from GMOS-S COS plotted in dot-dashed blue. All of the sources from GMOS-S COS were low QF sources.

5.2 Star Formation Rates

We use two of the emission line fluxes we measured, Hα and [OII]$_{\lambda3727}$, as star formation rate indicators. We calculate SFR$_{\mathrm{H}\alpha}$ and SFR$_{[\mathrm{OII}]_{\lambda3727}}$ using Equations 5 and 6. We calculate SFRs separately using the attenuated and unattenuated fluxes. In our sample, 36 sources had measurable Hα fluxes, and 87 sources had measurable [OII]$_{\lambda3727}$ emission. Only one source had both Hα and [OII]$_{\lambda3727}$ fluxes measured. We also used the SFRs as estimated by `MAGPHYS` through the SED modeling process described in Section 4.3. The uncorrected line SFRs and the SFRs from `MAGPHYS` are shown in Appendix A. Figure 17 shows a comparison of the SFRs as estimated using optical emission line fluxes to the SFRs derived from SED modeling. We plot the SFRs as estimated using both unattenuated and attenuated fluxes. The general trend we see for both Hα and [OII]$_{\lambda3727}$ is that the SFRs calculated with the unattenuated (uncorrected) fluxes are smaller than the SED SFRs and the fluxes corrected for attenuation are larger than the SED SFRs. This indicates that some degree of attenuation correction is most likely necessary to replicate the the SED SFRs but our prescription was too strong and resulted in an overcorrection. Another consideration for interpreting

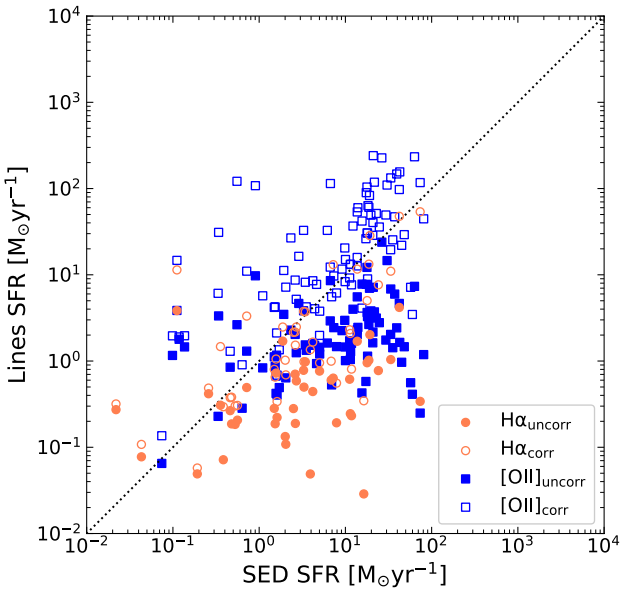

Figure 17: The SFR for each source as estimated from optical emission line fluxes as a function of the corresponding SFR from SED modeling with `MAGPHYS` The salmon circle points are SFRs calculated with the Hα emission line fluxes and the the blue square points are from [OII]$_{\lambda 3727}$ fluxes. Open shapes represent the SFR as calculated with an emission line flux that was corrected for attenuation, as described in Section 4.3. The filled shapes are SFRs derived from emission lines not corrected for attenuation. The black dotted line represents the 1-1 line of equal SFR estimates for the line method and the SFR derived from SED modeling.

this plot is that the different SFR estimators used (optical emission line fluxes versus SED modeling with `MAGPHYS`) are targeting different timescales of star formation so it is not unexpected that the two methods do not directly align. Optical emission line fluxes like Hα and the calibrated [OII]$_{\lambda 3727}$ indicator are probes of instantaneous star formation whereas `MAGPHYS` reports a total (UV+IR) SFR, as shown in Figure 5 in Section 1.5.5. In Figure 5, the line SFRs needed a larger attenuation correction to match up with the SED SFRs. To bring our line SFRs in agreement with our SED SFRs from MAGPHYS, we would have to adjust the amount of attenuation correction. For [OII]$_{\lambda 3727}$ SFRs, we would have the *decrease* the the correction by a factor of 1.37 to bring those SFRs in agreement with the SED SFRs. For Hα, we would have to *increase* the attenuation

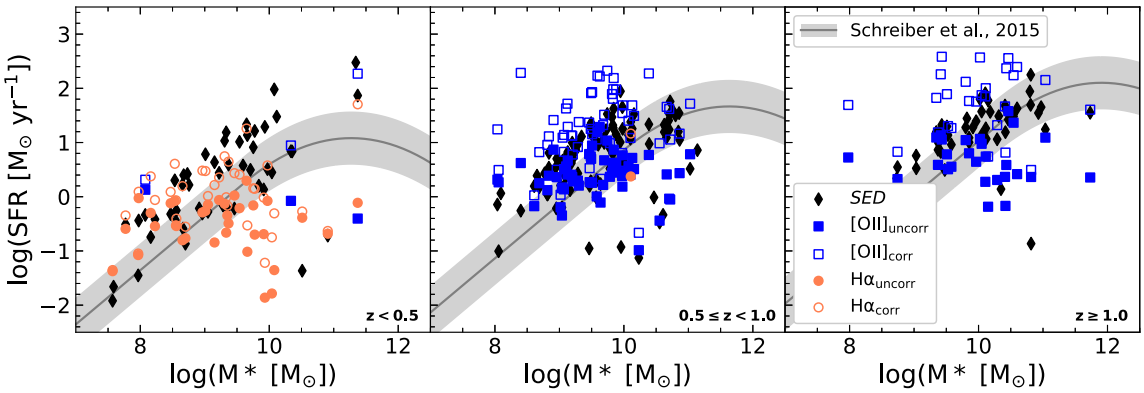

Figure 18: We show the SFRs as a function of stellar mass for three redshift ranges (z $<$ 0.5, 0.5 $<$ z $<$ 1.0, and z $>$ 1.0, from the left to right panels). The coloring for the emission line SFRs is the same as Figure 17 and then the black diamonds are for the SFRs from the MAGPHYS SED modeling. The gray shaded area encompassess a factor of three above and below the main sequence, from Schreiber et al. (2015).

correction by a factor of 0.72. This is similar to what was shown in Figure 5 from Wuyts et al. (2011), where the attenuation correction needed to be increased by a factor of 0.44 to bring the Hα into line with their SED SFRs. As a caveat, we recognize bringing the line SFRs into agreement with the SED SFRs is not quite physically appropriate, as line SFRs are probes of shorter timescales, and would be expected to be smaller than a more total SFR from the SED modeling. We therefore consider the additional correction factor for $H\alpha$ to be an upper limit.

We also shown the SFR (from emission line fluxes and SED modeling) as a function of stellar mass (from SED modeling) in Figure 18. As a point of comparison, we plot the main sequence from Schreiber et al. (2015) with a factor of 3$\times$ above and below from indicated by the shaded region. In all three redshift slices we show, our sources follow the main sequence with some above and below. Due to the diversity of our targeted sources, this is not unexpected. While two out of three projects targeted Herschel selected sources (see Section 2.1) and might be expected to have enhanced star formation, our sample also included a third project not targeting *Herschel* selected sources and all three projects included filler sources. For both emission line SFRs, the SFR calculated with the emission line luminosity corrected for attenuation is larger than the SFR from the line luminosity not corrected for attenuation. This is the same trend as shown in Figure 17. The panel with the

largest spread in SFRs is the left-most panel which shows sources with z < 0.5. In this redshift range, Hα is accessible for many of these sources, and the Hα SFRs tend to extend below the main sequence by up to a factor of 100. However, as discussed in Section 5.2, our Hα SFR measurements most likely need to be increased by a factor of 0.72, which would bring the corrected Hα SFRs back onto or above the main sequence.

5.3 AGN Classifications

Using our measured optical emission line fluxes, we used line diagnostics to identify AGN and compared those results to AGN classification of our sources with other methods. One reason AGN are important to study is that they are known to have a linkage to galaxies with elevated star formation (Elbaz et al., 2011; Kewley et al., 2006; Kauffmann et al., 2003). Two thirds of the observing projects included in this sample were targeting *Herschel*-selected (U)LIRGs which are known as a population to have a higher AGN fraction (Kartaltepe et al., 2010). The identification of AGN typically involves anaylsis of multiwavelength data, and the AGN identifications we made with our optical data can complement existing work and perhaps identify objects not previously identified as an AGN for future followup.

We make use of the broad multi-wavelength coverage available through CANDELS for our sources, allowing us to compare the results of multiple AGN classification techniques. We used the following four means of identifying AGN:

- A tradititional Baldwin, Philips, and Terlevich (BPT; Baldwin et al. 1981) diagram (Figure 19) to separate sources based on their main excitation mechanism (described in Section 1.6.3).
- A Mass Excitation (MeX; Juneau et al. 2011) diagram (Figure 20) to separate higher redshift sources based on the main excitation mechanism (described in Section 1.6.3).
- Flag in the CANDELS catalogs for X-ray identified AGN as those that have X-ray luminosities $> 10^{42}$ erg s^{-1} (Kocevski et al., 2018).
- Classification using an IRAC color-color diagram (Figure 20) from Donley et al. (2012) (described in Section 1.6.2).

The classifications of each object based on these four identification techniques is included in Appendix A. The first technique we used used was an optical diagnostic technique, the BPT diagram (Baldwin et al., 1981) to identify AGN. A BPT diagram plots a ratio of optical emission line on each axes in log space, and has empirically derived demarcation bounds that separate out sources based on their main excitation mechanism as discussed in Section 1.6.3. The BPT diagram separates sources into three regions. The left-most region is to the left of the Kauffmann et al. (2003) line, and contains star-forming sources. The right-most region is to the right of the Kewley et al. (2001) line, and contains AGN sources, or sources whose excitation is dominated by radiation from star-forming regions. Between these two lines are sources that are considered "composite" meaning they have mixed sources of ionization.

The four lines used to construct the classic BPT diagram are Hα, Hβ, [NII]$_{\lambda 6583}$, and [OIII]$_{\lambda 5007}$. Nine of our sources had measureable emission line fluxes for all four of these lines. There are only these few sources because the redshift of a galaxy to have all four lines is constrained by the redshift limit within Hα is detectable with an optical instrument (z < 0.4).

Based on the demarcation lines used for our BPT diagram, we have three sources classified as being dominated by star formation, five composite sources, and no AGN-dominated sources. Among our nine BPT sources, two of them were identified as an AGN with different techniques (as described below). The fact that no sources were identified as an AGN should not be generalized to our whole sample, as the number of sources included via BPT was less than 10% of the entire sample size, and only sources with $z < 0.4$.

For galaxies with a redshift of $z > 0.3$, we used the Mass Excitation (MeX; Juneau et al. (2011)) diagnostic to identify AGN. The construction of an MeX diagram is made by plotting [OIII]$_{\lambda 5007}$/Hβ as a function of stellar mass in log-log space. Stellar mass is used as a proxy for the [NII]$_{\lambda 6584}$/Hα axis used in the BPT diagram. The MeX diagram tends to have excellent agreement with the traditional BPT diagram, with the caveat that MeX-identified composite sources extend over both the composite and star-forming regions of a BPT diagram (see Figure 10 in Section 1.6.3). This means that a source identified as composite by the MeX diagram might actually be identified as star-forming with the BPT diagram (Juneau et al., 2011).

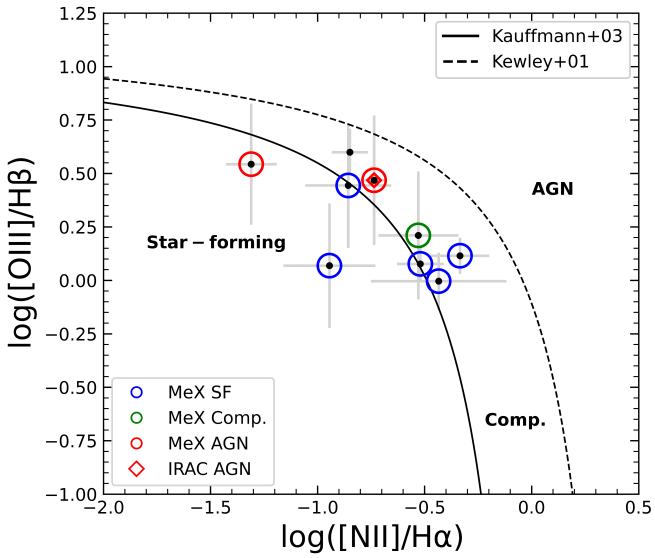

Figure 19: An optical diagnostic diagram (BPT) for the nine sources that have Hα, Hβ, [OIII], and [NII] measured emission line fluxes. The lower solid line is the semi-empirical line from Kauffmann et al. (2003), with star-forming galaxies lying below and to the left of this line. The dotted line is the maximum starburst line from Kewley et al. (2001), that marks the theoretical boundary separating AGN sources on the right. In between the two lines are the composite sources. The differently shaped colored points indicate the classification of a certain point from different AGN criteria, see Figure 20.

In the left panel of Figure 20, we show the MeX diagram for the 63 sources that had measured [OIII]$_{\lambda 5007}$ and Hβ emission line fluxes. Eight sources fall in the AGN region: one of the AGN-identified sources was classified as star-forming by the BPT diagram, one was classified as an X-ray AGN, one was identified as both a composite by the BPT diagram, and as an IR AGN, and the others were not identified as an AGN with any other techniques. None of the MeX-identified star-forming or composite sources were identified as an AGN with any other technique. In the right panel of Figure 20, we show the IRAC colors for our sample, with the selection wedge from Donley et al. (2012) outlined and colored in yellow. The Donley et al. (2012) selection criteria identified five sources in the IR selection region, but only one of those met all of the IR AGN selection criteria, including the constraint for monotonically increasing IRAC fluxes. That source was also identified as an AGN with the MeX diagram, and as a composite source with the BPT diagram. Five of the

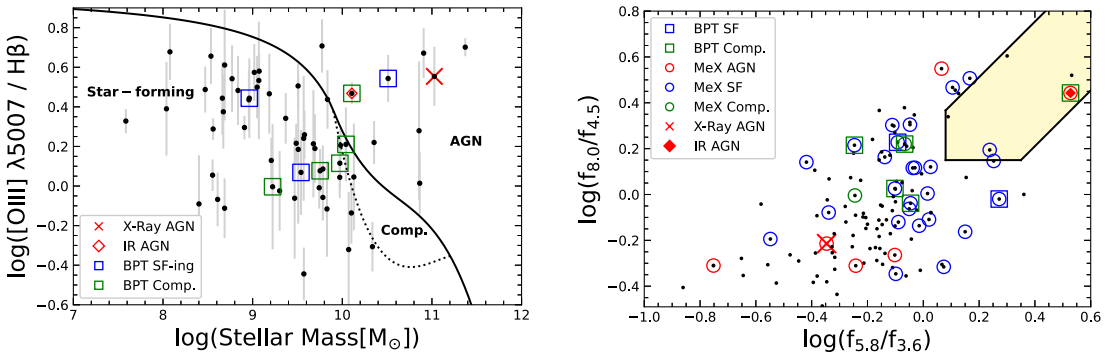

Figure 20: Left panel: The Mass Excitation (MeX; Juneau et al. 2011) including 63 of our sources. The ratio of $[\mathrm{OIII}]_{\lambda 5007}/H\beta$ is plotted as a function of stellar mass, which is a proxy for $[\mathrm{NII}]_{\lambda 6584}/\mathrm{H}\alpha$ which is used as the x-asis in a BPT Diagram. Identifications from other diagrams (Figure 19 and right panel of this Figure) are indicated by the legend. Right panel: The ratios of two IRAC bands are plotted against each other to identify IR AGN in this color space. The colored wedge indicates the region where AGN sources lie (Donley et al., 2012), and five of our sources are contained within there. Only one source, indicated with a red diamond, meets the full IR AGN criteria, including the monotonically increasing MIR slope.

sources not identified as an AGN within the IRAC color selection were identified as an AGN with other methods, four of those by the MeX and one of those by both the MeX and the X-ray flag.

6 Summary and Conclusions

In this thesis, we have presented the reduction process of Gemini/GMOS optical spectroscopic data taken of galaxies in two of the CANDELS fields that were lacking in spectroscopic coverage. We measured the redshifts of 196 galaxies from our observed sample, which have been shared with collaborators to use. These spectroscopic redshifts are particularly useful because they are more precise than existing photometric redshifts and can be used to better eliminate distance uncertainties when deriving distance-dependent properties of galaxies. Additionally, we measured the fluxes of several emission lines and used them to analyze the star formation rates of our galaxies and to identify AGN in our sample. Our results are summarized as follows:

- The correspondence between our measured spectroscopic redshifts and pre-existing photometric redshifts was good, with a mean dispersion (outliers removed) of 0.019 (0.017) for COS

(UDS). UDS did have a higher outlier fraction of 24.194% compared to the outlier fraction for COS which was 8.397%. However, UDS had a higher fraction of low QF redshifts compared to COS, and for both fields, the majority of outlier redshifts were low QF.

- SFRs derived from the emission lines Hα and [OII]$_{3727}$ did not strictly agree with the SFRs output by the SED modeling code, `MAGPHYS`. Using emission line luminosities not corrected for annenuation, the emission line SFRs were smaller than the SFRs from `MAGPHYS`. Including corrections for attenuation, the SFRs from the [OII] emission line were larger than the SFRs from `MAGPHYS`. We suspect this is a a result of the attenuation correction being overestimated by a factor of 1.37 for [OII] SFRs. We also estimated that our Hα SFRs were underestimated by a factor of 0.72, based on comparisions with the SED SFRs.

- We found that most of our sources lay on the main sequence, with some above, regardless of which SFR indicator is used. Since the sample includes *Herschel*-selected sources, it makes sense that many sources would lay on or above the main sequence. Sources that lay below the main sequence warrant followup.

- With the optical diagnostic BPT diagram, none of our sources were classified as an AGN, because none of them met the criteria based on their line ratio values. However, using the MeX diagram, nine sources were identified as an AGN, including seven that were not selected as such using IR colors or the X-ray flux. These sources could be followed up on to see if they are true AGN.

Acknowledgements

I would like to deeply thank my research advisor, Dr. Jeyhan Kartaltepe, for her support and expertise. I would also like to thank Dr. Ekta Shah, who was the second person to measure the redshifts for my sample. I would also like to sincerely thank Dr. Jeyhan Kartaltepe, Dr. Michael Lam and Dr. Andy Robinson for serving as my committee for this Master's thesis. Finally, I would like to thank my parents, my sister, and friends who have been great supports during this project.

References

Abdurro'uf, Accetta, K., Aerts, C., et al. 2022, , 259, 35

Antonucci, R. 1993, , 31, 473

Arnouts, S., Cristiani, S., Moscardini, L., et al. 1999, , 310, 540

Ashby, M. L. N., Willner, S. P., Fazio, G. G., et al. 2013, , 769, 80

Autry, R. G., Probst, R. G., Starr, B. M., et al. 2003, in Society of Photo-Optical Instrumentation Engineers (SPIE) Conference Series, Vol. 4841, Instrument Design and Performance for Optical/Infrared Ground-based Telescopes, ed. M. Iye & A. F. M. Moorwood, 525–539

Baldwin, J. A., Phillips, M. M., & Terlevich, R. 1981, , 93, 5

Bastian, N., Covey, K. R., & Meyer, M. R. 2010, , 48, 339

Bertelli, G., Bressan, A., Chiosi, C., Fagotto, F., & Nasi, E. 1994, , 106, 275

Bertin, E., & Arnouts, S. 1996, , 117, 393

Bolzonella, M., Miralles, J.-M., & Pello', R. 2000

Boquien, M., Burgarella, D., Roehlly, Y., et al. 2019, , 622, A103

Brammer, G. B., van Dokkum, P. G., & Coppi, P. 2008, , 686, 1503

Brammer, G. B., Sanchez-Janssen, R., Labbe, I., et al. 2012

Brandt, W. N., & Alexander, D. M. 2015, The Astronomy and Astrophysics Review, 23

Burgarella, D., Buat, V., & Iglesias-Páramo, J. 2005, , 360, 1413

Calzetti, D. 2012, Star Formation Rate Indicators, arXiv

Calzetti, D., Kinney, A. L., & Storchi-Bergmann, T. 1994, , 429, 582

Calzetti, D., Kennicutt, R. C., J., Bianchi, L., et al. 2005, , 633, 871

Calzetti, D., Kennicutt, R. C., Engelbracht, C. W., et al. 2007, , 666, 870

Calzetti, D., Wu, S. Y., Hong, S., et al. 2010, , 714, 1256

Cappellari, M., McDermid, R. M., Alatalo, K., et al. 2012, Nature, 484, 485

Carnall, A. C., McLure, R. J., Dunlop, J. S., & Davé , R. 2018, Monthly Notices of the Royal Astronomical Society, 480, 4379

Casali, M., Adamson, A., Alves de Oliveira, C., et al. 2007, , 467, 777

Chabrier, G. 2003, , 115, 763

Chabrier, G., & Baraffe, I. 1997, , 327, 1039

Chapman, S. C., Scott, D., Steidel, C. C., et al. 2000, , 319, 318

Charlot, S., & Bruzual, G. 1991, , 367, 126

Charlot, S., & Fall, S. M. 2000, , 539, 718

Charlot, S., & Longhetti, M. 2001, Monthly Notices of the Royal Astronomical Society, 323, 887

Chomiuk, L., & Povich, M. S. 2011

Cirasuolo, M., McLure, R. J., Dunlop, J. S., et al. 2007, , 380, 585

Civano, F., Marchesi, S., Comastri, A., et al. 2016, , 819, 62

Colless, M., Dalton, G., Maddox, S., et al. 2001, The 2dF Galaxy Redshift Survey: spectra and redshifts

Conroy, C. 2013, Annual Review of Astronomy and Astrophysics, 51, 393

da Cunha, E., Charlot, S., Dunne, L., Smith, D., & Rowlands, K. 2011, Proceedings of the International Astronomical Union, 7, 292–296

Dahlen, T., Mobasher, B., Faber, S. M., et al. 2013, The Astrophysical Journal, 775, 93

Davis, M., Guhathakurta, P., Konidaris, N. P., et al. 2007, , 660, L1

Dickey, C. M., Geha, M., Wetzel, A., & El-Badry, K. 2019, The Astrophysical Journal, 884, 180

Donley, J. L., Koekemoer, A. M., Brusa, M., et al. 2012, , 748, 142

Draine, B. T. 2003, Annual Review of Astronomy and Astrophysics, 41, 241

Elbaz, D., Daddi, E., Borgne, D. L., et al. 2007, Astronomy &amp Astrophysics, 468, 33

Elbaz, D., Dickinson, M., Hwang, H. S., et al. 2011, , 533, A119

Elvis, M., Civano, F., Vignali, C., et al. 2009, The Astrophysical Journal Supplement Series, 184, 158

Fazio, G. G., Hora, J. L., Allen, L. E., et al. 2004, , 154, 10

Furusawa, H., Kosugi, G., Akiyama, M., et al. 2008, , 176, 1

Galametz, A., Grazian, A., Fontana, A., et al. 2013, , 206, 10

Gardner, J. P., Mather, J. C., Clampin, M., et al. 2006, , 123, 485

Gemini Observatory, & AURA. 2016, Gemini IRAF: Data reduction software for the Gemini telescopes, Astrophysics Source Code Library, record ascl:1608.006

Giavalisco, M., Ferguson, H. C., Koekemoer, A. M., et al. 2004, , 600, L93

Gilli, R., Comastri, A., & Hasinger, G. 2006, Astronomy &amp Astrophysics, 463, 79

Gimeno, G., Roth, K., Chiboucas, K., et al. 2016, in Ground-based and Airborne Instrumentation for Astronomy VI, ed. C. J. Evans, L. Simard, & H. Takami, Vol. 9908, International Society for Optics and Photonics (SPIE), 872 – 885

Girardi, L., Bressan, A., Bertelli, G., & Chiosi, C. 2000, , 141, 371

Gordon, K. D., Misselt, K. A., Witt, A. N., & Clayton, G. C. 2001, The Astrophysical Journal, 551, 269

Griffin, M. J., Abergel, A., Abreu, A., et al. 2010, , 518, L3

Grogin, N. A., Kocevski, D. D., Faber, S. M., et al. 2011, The Astrophysical Journal Supplement Series, 197, 35

Gwyn, S. D. J. 2012, , 143, 38

Hickox, R. C., & Alexander, D. M. 2018, Annual Review of Astronomy and Astrophysics, 56, 625

Hook, I. M., Jørgensen, I., Allington-Smith, J. R., et al. 2004, , 116, 425

Hubble, E. 1929, Proceedings of the National Academy of Sciences, 15, 168

Ilbert, O., Arnouts, S., McCracken, H. J., et al. 2006, , 457, 841

Johnson, B. D., Leja, J., Conroy, C., & Speagle, J. S. 2021, , 254, 22

Juneau, S., Dickinson, M., Alexander, D. M., & Salim, S. 2011, , 736, 104

Kartaltepe, J. S., Sanders, D. B., Floc'h, E. L., et al. 2010, The Astrophysical Journal, 721, 98

Kauffmann, G., Heckman, T. M., Tremonti, C., et al. 2003, , 346, 1055

Kennicutt, Robert C., J. 1998, , 36, 189

Kennicutt, R. C., & Evans, N. J. 2012, , 50, 531

Kewley, L. J., Dopita, M. A., Sutherland, R. S., Heisler, C. A., & Trevena, J. 2001, , 556, 121

Kewley, L. J., Geller, M. J., & Jansen, R. A. 2004, , 127, 2002

Kewley, L. J., Geller, M. J., & Jansen, R. A. 2004, The Astronomical Journal, 127, 2002

Kewley, L. J., Geller, M. J., Jansen, R. A., & Dopita, M. A. 2002, , 124, 3135

Kewley, L. J., Groves, B., Kauffmann, G., & Heckman, T. 2006, , 372, 961

Kewley, L. J., Nicholls, D. C., & Sutherland, R. S. 2019, Annual Review of Astronomy and Astrophysics, 57, 511

Kirkpatrick, A., Pope, A., Sajina, A., et al. 2015, The Astrophysical Journal, 814, 9

Kocevski, D. D., Hasinger, G., Brightman, M., et al. 2018, The Astrophysical Journal Supplement Series, 236, 48

Koekemoer, A. M., Faber, S. M., Ferguson, H. C., et al. 2011, , 197, 36

Kroupa, P. 2001, , 322, 231

Lacy, M., Petric, A. O., Sajina, A., et al. 2007, , 133, 186

Lacy, M., Storrie-Lombardi, L. J., Sajina, A., et al. 2004, The Astrophysical Journal Supplement Series, 154, 166

Laidler, V. G., Papovich, C., Grogin, N. A., et al. 2007, , 119, 1325

Laigle, C., McCracken, H. J., Ilbert, O., et al. 2016, , 224, 24

Lawrence, A., Warren, S. J., Almaini, O., et al. 2007, , 379, 1599

Leitherer, C. 2005, in AIP Conference Proceedings (AIP)

Lewis, I., Balogh, M., De Propris, R., et al. 2002, , 334, 673

Li, A. 2008, Optical Properties of Dust, arXiv

Li, J.-T., & Wang, Q. D. 2013, , 428, 2085

Lilly, S. J., Fevre, O. L., Renzini, A., et al. 2007, The Astrophysical Journal Supplement Series, 172, 70

Lutz, D., Poglitsch, A., Altieri, B., et al. 2011, , 532, A90

Madau, P., & Dickinson, M. 2014, Annual Review of Astronomy and Astrophysics, 52, 415

Mannucci, F., Cresci, G., Maiolino, R., Marconi, A., & Gnerucci, A. 2010, , 408, 2115

Marchesi, S., Civano, F., Elvis, M., et al. 2016, , 817, 34

Marigo, P., Girardi, L., Bressan, A., et al. 2008, , 482, 883

Martin, D. C., Fanson, J., Schiminovich, D., et al. 2005, , 619, L1

Masters, D., & Capak, P. 2011, , 123, 638

McCracken, H. J., Milvang-Jensen, B., Dunlop, J., et al. 2012, Astronomy &amp Astrophysics, 544, A156

McLean, I. S., Steidel, C. C., Epps, H. W., et al. 2012, in Society of Photo-Optical Instrumentation Engineers (SPIE) Conference Series, Vol. 8446, Ground-based and Airborne Instrumentation for Astronomy IV, ed. I. S. McLean, S. K. Ramsay, & H. Takami, 84460J

Meynet, G., & Maeder, A. 2004, Astronomy &amp Astrophysics, 429, 581

Miyazaki, S., Komiyama, Y., Sekiguchi, M., et al. 2002, , 54, 833

Mobasher, B., Dahlen, T., Ferguson, H. C., et al. 2015, The Astrophysical Journal, 808, 101

Momcheva, I. G., Brammer, G. B., van Dokkum, P. G., et al. 2015

Moustakas, J., Robert C. Kennicutt, J., & Tremonti, C. A. 2006, The Astrophysical Journal, 642, 775

Nayyeri, H., Hemmati, S., Mobasher, B., et al. 2017, , 228, 7

Newman, J. A., Cooper, M. C., Davis, M., et al. 2013, The Astrophysical Journal Supplement Series, 208, 5

Noll, S., Burgarella, D., Giovannoli, E., et al. 2009, , 507, 1793

Norberg, P., Baugh, C. M., Hawkins, E., et al. 2002, , 332, 827

Novikov, I. D., & Thorne, K. S. 1973, in Black Holes (Les Astres Occlus), 343–450

Oliver, S. J., Bock, J., Altieri, B., et al. 2012, Monthly Notices of the Royal Astronomical Society, 424, 1614

Padovani, P., Alexander, D. M., Assef, R. J., et al. 2017, The Astronomy and Astrophysics Review, 25

Peterson, B. 2006, The Broad-Line Region in Active Galactic Nuclei, ed. D. Alloain, R. Johnson, & P. Lira (Berlin, Heidelberg: Springer Berlin Heidelberg), 77–100

Pietrinferni, A., Cassisi, S., Salaris, M., & Castelli, F. 2004, , 612, 168

Pilbratt, G. L., Riedinger, J. R., Passvogel, T., et al. 2010, , 518, L1

Poglitsch, A., Waelkens, C., Geis, N., et al. 2010, , 518, L2

Pozzetti, L., Bolzonella, M., Zucca, E., et al. 2010, , 523, A13

Rieke, G. H., Young, E. T., Engelbracht, C. W., et al. 2004, , 154, 25

Rosa-Gonzá lez, D., Terlevich, E., & Terlevich, R. 2002, Monthly Notices of the Royal Astronomical Society, 332, 283

Salim, S., & Narayanan, D. 2020, , 58, 529

Salpeter, E. E. 1955, , 121, 161

Sanders, D. B., & Mirabel, I. F. 1996, Annual Review of Astronomy and Astrophysics, 34, 749

Sanders, D. B., Salvato, M., Aussel, H., et al. 2007, , 172, 86

Santini, P., Ferguson, H. C., Fontana, A., et al. 2015, The Astrophysical Journal, 801, 97

Schaller, G., Schaerer, D., Meynet, G., & Maeder, A. 1992, , 96, 269

Schreiber, C., Pannella, M., Elbaz, D., et al. 2015, , 575, A74

Scoville, N., Aussel, H., Brusa, M., et al. 2007, , 172, 1

Shah, E. A., Kartaltepe, J. S., Magagnoli, C. T., et al. 2020, , 904, 107

Shakura, N. I., & Sunyaev, R. A. 1973, , 24, 337

Stern, D., Eisenhardt, P., Gorjian, V., et al. 2005, The Astrophysical Journal, 631, 163

Strateva, I., Ivezić, Ž., Knapp, G. R., et al. 2001, , 122, 1861

Sutherland, W., Emerson, J., Dalton, G., et al. 2015, Astronomy &amp Astrophysics, 575, A25

Taniguchi, Y., Kajisawa, M., Kobayashi, M. A. R., et al. 2015, Publications of the Astronomical Society of Japan, 67, 104

Tonry, J., & Davis, M. 1979, , 84, 1511

Treister, E., Urry, C. M., Duyne, J. V., et al. 2006, The Astrophysical Journal, 640, 603

Tremonti, C. A., Heckman, T. M., Kauffmann, G., et al. 2004, , 613, 898

Trumpler, R. J. 1930, , 42, 214

Tyler, K., Quillen, A. C., LaPage, A., & Rieke, G. H. 2004, The Astrophysical Journal, 610, 213

Urry, C. M., & Padovani, P. 1995, , 107, 803

Weaver, J. R., Kauffmann, O. B., Ilbert, O., et al. 2022, The Astrophysical Journal Supplement Series, 258, 11

Werner, M. W., Roellig, T. L., Low, F. J., et al. 2004, The Astrophysical Journal Supplement Series, 154, 1

Wesson, R. 2016, , 456, 3774

Whitaker, K. E., Labbé , I., van Dokkum, P. G., et al. 2011, The Astrophysical Journal, 735, 86

Wuyts, S., Schreiber, N. M. F., Lutz, D., et al. 2011, The Astrophysical Journal, 738, 106

Xiao, M.-Y., Zhao, Y., Gu, Q.-S., & Shi, Y. 2018, The Astrophysical Journal, 854, 111

York, D. G., Adelman, J., Anderson, J. E., et al. 2000, Box 1149, Flagstaff, AZ 86002-1149 19 U.S. Naval Observatory, 3450 Massachusetts Ave

A Appendix A

Table 8: The properties of our sources, including identification information, the measured spectroscopic redshifts and their associated quality flags, and the SFRs and AGN classifications. We show the SFRs from the two emission lines we used, Hα and [OII]$_{\lambda 3727}$, which are the uncalibrated values (see Section 4.3 for a discussion on the attenuation corrections). We also show the AGN flags based on the four different classification systems we used, as discussed in Section 5.3. A value of 1 indicates that source was identified as an AGN with that detection technique, a value of 0 means that it was not, and the absence of a classification means that the necessary data for that technique was not available.

					SFRs [$M_\odot$ yr^{-1}]			**AGN Flags**			
Program	**Ra**	**Dec**	**spec-z**	**QF**	**Hα**	**[OII]$_{\lambda 3727}$**	**MAGPHYS**	**MeX**	**IRAC**	**X-ray**	**BPT**
COS-N	150.1212	2.4855	0.6479	4	–	2.33±0.24	$7.89^{+3.76}_{-1.72}$	1	0	–	–
COS-N	150.1803	2.4981	0.648	3	–	–	$3.93^{+1.14}_{-0.26}$	–	–	–	–
COS-N	150.1827	2.5123	0.6788	3	–	1.37±0.17	$1.53^{+3.01}_{-0.11}$	1	–	–	–
COS-N	150.1993	2.5222	0.896	2	–	0.78±0.20	$1.71^{+0.44}_{-0.37}$	–	–	–	–
COS-N	150.1912	2.5246	0.5079	4	–	1.01±0.14	$2.04^{+0.63}_{-0.24}$	1	0	–	–
COS-N	150.1410	2.5308	0.896	2	–	3.44±0.21	$20.87^{+4.39}_{-2.27}$	1	0	–	–
COS-N	150.1604	2.5346	0.936	1	–	2.78±0.29	$29.46^{+9.94}_{-7.42}$	–	0	–	–
COS-N	150.1688	2.5445	0.789	1	–	0.89±0.18	$57.08^{+0.65}_{-46.21}$	–	0	–	–
COS-N	150.0936	2.4809	0.936	1	–	–	$0.97^{+3.04}_{-3.28}$	–	–	–	–
COS-N	150.1177	2.5086	0.936	2	–	19.34±1.96	$17.78^{+4.84}_{-5.12}$	–	0	–	–
COS-N	150.1923	2.4079	1.1494	2	–	0.68±0.09	$15.54^{+3.58}_{-4.16}$	–	0	–	–
COS-N	150.1873	2.4143	0.851	4	–	1.54±0.10	$44.91^{+19.08}_{-12.88}$	–	0	–	–
COS-N	150.1814	2.4234	0.7281	4	–	6.07±0.21	$3.27^{+0.40}_{-1.18}$	3	0	1	–
COS-N	150.1951	2.4313	0.977	2	–	2.31±0.19	$9.93^{+4.15}_{-1.87}$	–	0	–	–

Table 8 continued from previous page

					SFRs [$M_\odot$ yr^{-1}]			AGN Flags			
	Ra	**Dec**	**spec-z**	**QF**	**Hα**	**[OII]$_{\lambda3727}$**	**MAGPHYS**	**MeX**	**IRAC**	**X-ray**	**BPT**
COS-N	150.1619	2.4472	0.94	3	–	1.65±0.17	$11.41^{+1.49}_{-2.66}$	1	0	–	–
COS-N	150.1551	2.4435	1.3596	1	–	2.27±0.20	$35.42^{+3.04}_{-27.76}$	–	0	–	–
COS-N	150.1374	2.4489	1.17	2	–	3.21±0.34	$13.71^{+8.27}_{-4.70}$	–	0	–	–
COS-N	150.1452	2.4555	1.22	1	–	1.88±0.27	$80.83^{+5.79}_{-4.87}$	–	0	–	–
COS-N	150.1844	2.4594	1.438	1	–	2.04±0.30	$11.49^{+3.04}_{-3.28}$	–	0	–	–
COS-N	150.1779	2.4582	0.5981	2	–	–	$0.46^{+0.05}_{-3.28}$	–	0	–	–
COS-N	150.0996	2.3798	0.892	1	–	5.89±0.90	$21.69^{+4.39}_{-0.25}$	–	0	–	–
COS-N	150.1150	2.3810	1.1443	1	–	12.31±1.41	$17.46^{+0.20}_{-3.59}$	–	0	–	–
COS-N	150.0516	2.4073	0.937	2	–	–	$19.22^{+7.74}_{-3.78}$	–	0	–	–
COS-N	150.0546	2.4319	0.441	4	–	1.35±0.41	$0.46^{+0.22}_{-0.08}$	1	–	–	–
COS-N	150.1647	2.3228	0.774	4	–	2.55±0.18	$11.77^{+0.27}_{-1.72}$	1	0	–	–
COS-N	150.1621	2.3247	0.855	1	–	–	$12.91^{+3.04}_{-5.75}$	–	–	–	–
COS-N	150.1983	2.3261	0.2575	3	0.14±0.02	–	$4.33^{+0.73}_{-2.53}$	–	0	–	–
COS-N	150.1507	2.3387	0.852	4	–	2.54±0.24	$4.19^{+1.08}_{-1.21}$	1	–	–	–
COS-N	150.1922	2.3458	0.599	4	–	2.42±0.16	$4.40^{+1.11}_{-0.42}$	1	0	–	–
COS-N	150.1453	2.3696	0.729	4	–	1.78±0.23	$1.50^{+0.48}_{-0.20}$	1	–	–	–
COS-N	150.1261	2.3166	0.885	1	–	4.64±0.54	$6.67^{+0.88}_{-2.44}$	–	–	–	–

Table 8 continued from previous page

					SFRs [$M_\odot$ yr^{-1}]			AGN Flags			
	Ra	**Dec**	**spec-z**	**QF**	**Hα**	**[OII]$_{\lambda3727}$**	**MAGPHYS**	**MeX**	**IRAC**	**X-ray**	**BPT**
COS-N	150.1007	2.3202	1.24	2	–	–	$27.84^{+6.19}_{-4.42}$	–	–	–	–
COS-N	150.0932	2.3208	0.38	1	0.84±0.03	–	$3.23^{+0.41}_{-0.33}$	1	0	–	2
COS-N	150.1205	2.3215	0.495	3	–	–	$2.63^{+1.07}_{-0.35}$	–	0	–	–
COS-N	150.1285	2.3298	1.0821	2	–	–	$13.79^{+8.93}_{-2.55}$	–	0	–	–
COS-N	150.0590	2.3416	0.732	3	–	1.60±0.25	$10.02^{+4.50}_{-1.05}$	1	0	–	–
COS-N	150.1170	2.3419	1.189	1	–	3.58±0.42	$9.14^{+4.39}_{-2.60}$	–	–	–	–
COS-N	150.1555	2.2055	0.776	4	–	–	$25.40^{+1.19}_{-3.00}$	–	0	–	–
COS-N	150.1210	2.2083	0.982	4	–	5.20±0.40	$18.04^{+1.97}_{-3.28}$	2	0	–	–
COS-N	150.1845	2.2088	1.41	1	–	9.48±0.56	$37.30^{+11.62}_{-11.44}$	–	–	–	–
COS-N	150.1996	2.2193	0.878	4	–	3.66±0.35	$13.70^{+2.03}_{-2.50}$	1	0	–	–
COS-N	150.1873	2.2224	0.244	4	0.71±0.06	–	$0.53^{+0.12}_{-0.10}$	–	0	–	2
COS-N	150.1691	2.2339	1.242	2	–	–	$36.74^{+8.49}_{-7.48}$	–	0	–	–
COS-N	150.2020	2.2372	1.242	1	–	3.85±0.90	$39.35^{+0.91}_{-11.09}$	–	0	–	–
COS-N	150.1525	2.2445	1.22	2	–	6.06±0.52	$19.75^{+1.74}_{-1.97}$	–	0	–	–
COS-N	150.1322	2.2509	0.438	4	–	0.84±0.26	$6.92^{+0.57}_{-0.62}$	1	0	–	–
COS-N	150.1349	2.2582	0.784	4	–	–	$1.32^{+0.38}_{-0.22}$	–	–	–	–
COS-N	150.1411	2.2171	0.22	2	0.17±0.01	–	$0.14^{+0.03}_{-0.03}$	–	0	–	–

Table 8 continued from previous page

					SFRs [$M_\odot$ yr^{-1}]			AGN Flags			
	Ra	**Dec**	**spec-z**	**QF**	**Hα**	**[OII]$_{\lambda3727}$**	**MAGPHYS**	**MeX**	**IRAC**	**X-ray**	**BPT**
COS-N	150.1119	2.2173	0.373	4	0.76±0.05	–	$0.48^{+0.07}_{-0.11}$	1	–	–	–
COS-N	150.1283	2.2189	0.839	2	–	5.00±0.36	$22.82^{+7.72}_{-1.00}$	–	0	–	–
COS-N	150.1035	2.2214	0.662	3	–	1.92±0.38	$5.03^{+2.20}_{-0.87}$	1	0	–	–
COS-N	150.1012	2.2320	0.751	4	–	3.23±0.28	$2.62^{+0.80}_{-0.27}$	1	0	–	–
COS-N	150.1093	2.2333	0.851	4	–	1.86±0.22	$1.59^{+1.38}_{-0.63}$	1	–	–	–
COS-N	150.0899	2.2349	0.838	1	–	0.92±0.29	$17.29^{+3.04}_{-0.97}$	–	0	–	–
COS-N	150.0936	2.2372	1.436	2	–	–	$34.99^{+8.18}_{-5.62}$	–	0	–	–
COS-N	150.1233	2.2533	0.3821	4	0.29±0.03	–	$0.56^{+0.10}_{-0.11}$	1	–	–	–
COS-N	150.0737	2.2627	0.98	2	–	1.98±0.37	$2.69^{+0.96}_{-0.58}$	–	–	–	–
COS-N	150.0865	2.2643	0.749	2	–	–	$6.44^{+1.12}_{-3.28}$	–	0	–	–
COS-N	150.1692	2.4723	0.686	4	–	5.52±0.52	$1.93^{+0.50}_{-0.32}$	1	–	–	–
COS-N	150.1581	2.4747	0.887	1	–	–	$10.15^{+0.92}_{-1.22}$	–	0	–	–
COS-N	150.1172	2.4775	0.626	4	–	–	$1.88^{+3.04}_{-0.94}$	1	–	–	–
COS-N	150.1389	2.4782	0.897	2	–	3.23±0.55	$33.45^{+17.71}_{-6.18}$	–	0	–	–
COS-N	150.1816	2.4890	1.164	2	–	23.21±1.58	$30.42^{+3.04}_{-8.86}$	–	0	–	–
COS-N	150.1534	2.5026	1.175	2	–	–	$18.99^{+5.06}_{-4.27}$	–	–	–	–
COS-N	150.1286	2.5027	1.174	2	–	13.58±0.71	$6.70^{+5.50}_{-0.59}$	–	0	–	–

Table 8 continued from previous page

					SFRs [$M_\odot$ yr^{-1}]			AGN Flags			
	Ra	**Dec**	**spec-z**	**QF**	**Hα**	**[OII]$_{\lambda3727}$**	**MAGPHYS**	**MeX**	**IRAC**	**X-ray**	**BPT**
COS-N	150.1262	2.5091	1.143	2	–	–	$10.09^{+10.94}_{-3.28}$	–	0	–	–
COS-N	150.1418	2.5289	1.318	2	–	37.92±3.02	$26.44^{+5.79}_{-2.22}$	–	0	–	–
COS-N	150.1606	2.5318	0.849	3	–	10.86±0.77	$33.57^{+14.51}_{-5.43}$	1	0	–	–
COS-N	150.1053	2.4624	0.377	4	0.30±0.02	–	$0.36^{+0.21}_{-0.04}$	1	0	–	–
COS-N	150.0674	2.4736	0.614	4	–	0.67±0.18	$1.57^{+3.04}_{-0.95}$	1	0	–	–
COS-N	150.0634	2.4796	0.987	2	–	2.84±0.44	$0.12^{+0.01}_{-3.28}$	–	0	–	–
COS-N	150.0580	2.4831	0.731	2	–	–	$12.28^{+0.87}_{-3.28}$	–	0	–	–
COS-N	150.0637	2.4855	0.25	2	0.08±0.01	–	$0.04^{+0.02}_{-0.03}$	–	–	–	–
COS-N	150.0734	2.4878	1.162	2	–	5.51±0.59	$18.28^{+17.99}_{-27.11}$	–	0	–	–
COS-N	150.0837	2.4942	0.73	4	–	1.48±0.13	$4.63^{+0.05}_{-0.68}$	1	–	–	–
COS-N	150.0689	2.5004	1.44	2	–	–	$11.70^{+2.23}_{-3.09}$	–	–	–	–
COS-N	150.0575	2.5074	1.159	2	–	4.42±0.29	$24.75^{+1.16}_{-4.38}$	–	0	–	–
COS-N	150.1346	2.5137	0.731	4	–	–	$0.61^{+0.14}_{-0.12}$	–	–	–	–
COS-N	150.1118	2.5433	0.725	4	–	–	$2.70^{+0.52}_{-0.29}$	1	0	–	–
COS-N	150.1514	2.3933	1.405	2	–	–	$49.49^{+4.18}_{-6.42}$	–	0	–	–
COS-N	150.1970	2.3953	0.667	2	–	–	$0.98^{+0.05}_{-3.28}$	1	0	–	–
COS-N	150.1678	2.3967	0.69	1	–	–	$15.62^{+3.35}_{-1.97}$	–	0	–	–

Table 8 continued from previous page

					SFRs [$M_\odot$ yr^{-1}]			AGN Flags			
	Ra	**Dec**	**spec-z**	**QF**	**Hα**	**[OII]$_{\lambda3727}$**	**MAGPHYS**	**MeX**	**IRAC**	**X-ray**	**BPT**
COS-N	150.1854	2.3984	1.299	2	–	–	$87.68^{+5.13}_{-3.89}$	–	0	–	–
COS-N	150.2029	2.3991	0.929	4	–	6.13±0.70	$0.11^{+0.19}_{-0.17}$	–	–	–	–
COS-N	150.1766	2.4012	0.832	2	–	–	$19.12^{+14.90}_{-3.28}$	–	0	–	–
COS-N	150.1915	2.4157	0.8885	4	–	8.81±0.68	$13.72^{+1.15}_{-0.62}$	1	0	–	–
COS-N	150.1293	2.4207	1.05	2	–	–	$9.85^{+1.99}_{-3.28}$	–	–	–	–
COS-N	150.1320	2.4391	1.128	2	–	11.08±1.49	$19.03^{+6.64}_{-2.69}$	–	0	–	–
COS-N	150.1244	2.4515	1.198	2	–	–	$3.12^{+3.04}_{-3.28}$	–	–	–	–
COS-N	150.1113	2.3893	0.322	4	0.45±0.03	–	$0.61^{+0.12}_{-0.12}$	–	0	–	–
COS-N	150.0727	2.4113	0.906	2	–	–	$7.23^{+3.04}_{-3.28}$	–	–	–	–
COS-N	150.1385	2.4209	0.334	4	0.84±0.06	–	$2.01^{+0.34}_{-0.05}$	1	–	–	–
COS-N	150.0703	2.4230	0.747	4	–	5.80±0.37	$17.86^{+0.18}_{-2.44}$	1	0	–	–
COS-N	150.0933	2.4492	1.181	1	–	–	$2.18^{+3.04}_{-3.28}$	–	–	–	–
COS-N	150.0783	2.4526	0.538	4	–	0.64±0.16	$1.61^{+3.04}_{-0.66}$	1	–	–	–
COS-N	150.1764	2.2970	0.852	4	–	4.21±0.30	$18.71^{+6.24}_{-13.49}$	1	–	–	–
COS-N	150.1323	2.3004	0.498	3	–	–	$2.50^{+0.15}_{-0.09}$	1	–	–	–
COS-N	150.1595	2.3018	0.372	3	1.05±0.16	–	$0.61^{+0.15}_{-0.13}$	–	–	–	–
COS-N	150.1403	2.3021	0.94	2	–	–	$6.25^{+2.52}_{-1.26}$	–	0	–	–

Table 8 continued from previous page

					SFRs [$M_\odot$ yr^{-1}]			AGN Flags			
	Ra	**Dec**	**spec-z**	**QF**	**Hα**	**[OII]$_{\lambda3727}$**	**MAGPHYS**	**MeX**	**IRAC**	**X-ray**	**BPT**
COS-N	150.1642	2.3066	0.886	4	–	2.44±0.24	$3.43^{+1.46}_{-0.22}$	1	–	–	–
COS-N	150.1790	2.3125	0.101	2	0.04±0.00	–	$0.01^{+0.01}_{-0.01}$	–	0	–	–
COS-N	150.1948	2.3118	0.892	2	–	–	$38.43^{+8.26}_{-6.06}$	–	0	–	–
COS-N	150.1349	2.3406	1.071	2	–	6.33±0.71	$12.25^{+4.26}_{-1.94}$	–	–	–	–
COS-N	150.1692	2.3550	0.688	4	–	–	$3.31^{+2.25}_{-0.91}$	1	0	–	–
COS-N	150.1212	2.2859	0.986	2	–	–	$9.11^{+3.04}_{-3.28}$	–	0	–	–
COS-N	150.0865	2.2862	1.261	1	–	11.67±1.09	$63.31^{+10.28}_{-4.16}$	–	0	–	–
COS-N	150.1269	2.3015	0.374	4	0.51±0.02	–	$0.49^{+0.04}_{-0.04}$	1	0	–	1
COS-N	150.0590	2.3024	0.939	2	–	–	$33.23^{+7.16}_{-5.19}$	–	0	–	–
COS-N	150.1114	2.3050	0.496	4	–	–	$0.26^{+0.03}_{-0.02}$	1	–	–	–
COS-N	150.0997	2.3059	0.95	2	–	3.90±0.45	$13.96^{+3.04}_{-0.78}$	–	–	–	–
COS-N	150.1246	2.3444	0.925	2	–	2.57±0.38	$6.17^{+2.10}_{-1.94}$	–	0	–	–
COS-N	150.0718	2.3610	0.907	3	–	–	$34.84^{+4.84}_{-1.02}$	3	0	–	–
COS-N	150.2005	2.2183	0.88	3	–	–	$15.90^{+1.40}_{-2.30}$	–	0	–	–
COS-N	150.1417	2.2232	0.952	2	–	4.70±0.50	$9.84^{+1.93}_{-1.33}$	1	–	–	–
COS-N	150.1224	2.2463	0.249	4	0.29±0.01	–	$0.38^{+0.03}_{-0.01}$	–	–	–	–
COS-N	150.1678	2.2471	0.868	2	–	2.58±0.48	$20.77^{+0.70}_{-2.59}$	–	0	–	–

Table 8 continued from previous page

					SFRs [$M_\odot$ yr^{-1}]			AGN Flags			
	Ra	**Dec**	**spec-z**	**QF**	**Hα**	**[OII]$_{\lambda3727}$**	**MAGPHYS**	**MeX**	**IRAC**	**X-ray**	**BPT**
COS-N	150.1201	2.2543	1.032	2	–	3.87±0.54	$7.34^{+1.31}_{-1.16}$	–	0	–	–
COS-N	150.1757	2.2656	1.17	2	–	12.38±0.66	$15.60^{+3.48}_{-5.05}$	–	0	–	–
COS-N	150.1844	2.2740	0.926	2	–	–	$31.67^{+1.74}_{-0.83}$	–	0	–	–
COS-N	150.1844	2.2740	0.461	4	–	–	$6.84^{+0.74}_{-0.78}$	3	0	–	–
COS-N	150.1193	2.1879	0.877	2	–	–	$21.27^{+1.98}_{-4.22}$	–	0	–	–
COS-N	150.0575	2.2018	1.143	2	–	–	$177.70^{+31.39}_{-51.45}$	–	0	–	–
UDS-S	34.5278	-5.2055	1.455	1	–	2.31±0.42	$0.14^{+3.04}_{-3.28}$	–	–	–	–
UDS-S	34.5181	-5.1991	0.356	4	0.21±0.01	–	$0.19^{+3.04}_{-3.28}$	3	–	–	–
UDS-S	34.5046	-5.1851	0.388	3	0.62±0.03	–	$10.30^{+7.53}_{-4.78}$	1	0	–	1
UDS-S	34.5363	-5.1768	0.431	4	0.77±0.03	0.40±0.08	$73.61^{+0.84}_{-18.83}$	3	0	–	–
UDS-S	34.5105	-5.1949	0.144	1	–	–	$1.60^{+0.63}_{-0.30}$	–	0	–	–
UDS-S	34.5643	-5.1800	0.346	4	0.02±0.00	–	$2.81^{+1.17}_{-0.84}$	2	0	–	2
UDS-S	34.5631	-5.1698	0.9195	2	–	0.10±0.01	$0.07^{+3.04}_{-0.04}$	–	0	–	–
UDS-S	34.3195	-5.2097	0.7595	3	–	2.72±0.38	$11.20^{+2.60}_{-2.75}$	3	0	–	–
UDS-S	34.3992	-5.1954	0.646	4	–	2.29±0.39	$5.02^{+2.10}_{-0.75}$	1	0	–	–
UDS-S	34.3508	-5.1899	0.367	1	0.94±0.09	–	$0.36^{+0.10}_{-0.03}$	–	0	–	–
UDS-S	34.3472	-5.1758	0.383	1	–	–	$3.13^{+0.91}_{-0.71}$	–	0	–	–

Table 8 continued from previous page

					SFRs [$M_\odot$ yr^{-1}]			AGN Flags			
	Ra	**Dec**	**spec-z**	**QF**	**Hα**	**[OII]$_{\lambda3727}$**	**MAGPHYS**	**MeX**	**IRAC**	**X-ray**	**BPT**
UDS-S	34.3588	-5.1739	1.551	1	–	–	$1.05^{+2.10}_{-2.93}$	–	0	–	–
UDS-S	34.3775	-5.2137	0.787	4	–	4.18±0.73	$0.55^{+0.04}_{-2.93}$	1	0	–	–
UDS-S	34.2628	-5.2013	0.921	1	–	–	$1.16^{+0.01}_{-0.01}$	–	0	–	–
UDS-S	34.2450	-5.1846	0.626	4	–	–	$10.44^{+1.82}_{-2.93}$	1	0	–	–
UDS-S	34.2509	-5.1798	0.3475	3	0.20±0.01	–	$16.34^{+3.54}_{-1.15}$	3	–	–	–
UDS-S	34.2505	-5.1627	0.832	1	–	–	$2.45^{+0.46}_{-0.56}$	–	0	–	–
UDS-S	34.2380	-5.1489	0.388	1	0.16±0.02	–	$1.68^{+2.10}_{-0.02}$	–	0	–	–
UDS-S	34.2625	-5.1393	0.94	1	–	–	$3.98^{+0.05}_{-2.93}$	–	0	–	–
UDS-S	34.5330	-5.2563	0.751	2	–	–	$7.22^{+2.10}_{-2.93}$	–	0	–	–
UDS-S	34.5054	-5.2538	0.353	4	0.41±0.01	–	$0.04^{+2.10}_{-2.93}$	3	0	–	1
UDS-S	34.5109	-5.2522	0.351	4	0.22±0.01	–	$15.41^{+2.10}_{-6.73}$	–	0	–	–
UDS-S	34.5363	-5.2501	1.147	2	–	2.33±0.28	$48.15^{+8.90}_{-28.00}$	–	0	–	–
UDS-S	34.5271	-5.2434	0.342	3	0.26±0.01	–	$0.31^{+0.13}_{-0.03}$	–	0	–	–
UDS-S	34.5418	-5.2286	0.299	1	0.04±0.01	–	$95.51^{+7.78}_{-59.03}$	–	0	–	–
UDS-S	34.5892	-5.2215	0.93	2	–	–	$2.96^{+2.10}_{-2.93}$	–	0	–	–
UDS-S	34.5456	-5.2184	0.6154	1	–	–	$88.19^{+13.76}_{-4.02}$	–	0	–	–
UDS-S	34.5242	-5.2186	0.113	1	0.01±0.00	–	$19.44^{+2.10}_{-7.83}$	–	–	–	–

Table 8 continued from previous page

					SFRs [$M_\odot$ yr^{-1}]			AGN Flags			
	Ra	**Dec**	**spec-z**	**QF**	**Hα**	**[OII]$_{\lambda3727}$**	**MAGPHYS**	**MeX**	**IRAC**	**X-ray**	**BPT**
UDS-S	34.4570	-5.2238	0.1393	2	–	–	$1.65^{+0.80}_{-0.54}$	–	0	–	–
UDS-S	34.4385	-5.2199	0.2897	2	0.20±0.03	–	$1.36^{+0.31}_{-0.35}$	–	0	–	–
UDS-S	34.4709	-5.1984	1.631	2	–	2.61±0.46	$42.67^{+14.37}_{-7.48}$	–	0	–	–
UDS-S	34.4672	-5.1918	1.415	1	–	–	$1.38^{+0.02}_{-0.09}$	–	0	–	–
UDS-S	34.3686	-5.2508	0.306	3	–	–	$0.69^{+2.10}_{-2.93}$	–	0	–	–
UDS-S	34.3791	-5.2419	1.427	2	–	–	$3.35^{+0.87}_{-0.95}$	–	0	–	–
UDS-S	34.3626	-5.2178	0.305	3	–	–	$0.61^{+2.10}_{-2.93}$	–	0	–	–
UDS-S	34.2540	-5.2691	0.448	2	0.50±0.15	–	$0.18^{+0.00}_{-0.01}$	–	0	–	–
UDS-S	34.2683	-5.2716	0.3475	4	–	–	$0.02^{+0.01}_{-0.01}$	1	0	–	–
UDS-S	34.2235	-5.2377	0.716	3	–	15.45±1.11	$0.90^{+0.19}_{-0.15}$	–	0	–	–
UDS-S	34.2433	-5.2205	0.348	3	–	–	$298.70^{+2.10}_{-2.93}$	–	0	–	–
UDS-S	34.5796	-5.1800	0.259	2	–	–	$3.76^{+4.24}_{-3.26}$	–	0	–	–
UDS-S	34.5648	-5.1689	0.497	1	0.87±0.06	–	$2.76^{+0.49}_{-0.24}$	1	0	–	2
UDS-S	34.5870	-5.1460	0.235	2	–	–	$30.04^{+7.06}_{-3.07}$	–	0	–	–
UDS-S	34.4309	-5.2062	0.912	2	–	1.32±0.14	$1.10^{+0.34}_{-0.17}$	–	0	–	–
UDS-S	34.4150	-5.2001	0.67	2	–	0.45±0.11	$0.63^{+2.10}_{-2.93}$	–	0	–	–
UDS-S	34.4242	-5.1926	0.493	1	0.69±0.03	–	$8.18^{+1.14}_{-1.25}$	1	0	–	2

Table 8 continued from previous page

					SFRs [$M_\odot$ yr^{-1}]			AGN Flags			
	Ra	**Dec**	**spec-z**	**QF**	**Hα**	**[OII]$_{\lambda3727}$**	**MAGPHYS**	**MeX**	**IRAC**	**X-ray**	**BPT**
UDS-S	34.4126	-5.1907	0.878	4	–	1.81±0.32	$18.08^{+1.59}_{-1.28}$	1	0	–	–
UDS-S	34.4834	-5.1828	0.4575	3	0.74±0.04	–	$10.77^{+2.78}_{-3.39}$	–	0	–	–
UDS-S	34.4360	-5.1700	0.347	4	0.32±0.03	–	$3.92^{+2.10}_{-2.93}$	1	0	–	–
UDS-S	34.3476	-5.1957	0.916	2	–	–	$9.40^{+2.29}_{-2.86}$	–	0	–	–
UDS-S	34.3434	-5.1610	1.01	2	–	5.29±0.96	$0.34^{+0.08}_{-0.16}$	–	0	–	–
UDS-S	34.3639	-5.1594	0.476	2	1.97±0.12	–	$21.65^{+6.34}_{-2.44}$	–	–	–	–
UDS-S	34.2594	-5.1747	0.919	1	–	–	$3.94^{+0.95}_{-0.99}$	–	0	–	–
UDS-S	34.2355	-5.1610	1.013	1	–	11.37±0.82	$21.05^{+0.94}_{-1.12}$	–	0	–	–
UDS-S	34.5610	-5.2600	0.509	4	2.37±0.13	–	$24.12^{+2.10}_{-3.59}$	3	1	–	2
UDS-S	34.5455	-5.2517	0.924	1	–	0.36±0.08	$0.33^{+1.81}_{-3.07}$	–	–	–	–
UDS-S	34.5743	-5.2297	0.708	4	–	3.62±0.52	$2.33^{+0.74}_{-0.43}$	–	0	–	–
UDS-S	34.5888	-5.1972	1.0275	1	–	2.12±0.13	$3.52^{+0.24}_{-0.49}$	–	0	–	–
UDS-S	34.4181	-5.2566	1.398	1	–	–	$14.97^{+5.42}_{-2.93}$	–	0	–	–
UDS-S	34.4331	-5.1909	0.984	1	–	2.07±0.36	$0.72^{+0.01}_{-0.55}$	1	–	–	–
UDS-S	34.3233	-5.2674	0.2685	2	0.10±0.01	–	$13.70^{+1.45}_{-4.19}$	–	–	–	–
UDS-S	34.3748	-5.2275	1.428	2	–	–	$30.69^{+7.67}_{-5.82}$	–	0	–	–
UDS-S	34.3626	-5.2178	0.306	2	0.55±0.01	–	$6.07^{+0.14}_{-0.14}$	–	0	–	–

Table 8 continued from previous page

					SFRs [$M_\odot$ yr^{-1}]			AGN Flags			
	Ra	**Dec**	**spec-z**	**QF**	**Hα**	**[OII]$_{\lambda3727}$**	**MAGPHYS**	**MeX**	**IRAC**	**X-ray**	**BPT**
UDS-S	34.3708	-5.2145	0.912	2	–	7.39±0.39	$2.88^{+1.02}_{-0.66}$	1	0	–	–
COS-S	150.1166	2.5119	0.5915	1	–	–	$5.81^{+1.75}_{-1.50}$	–	0	–	–
COS-S	150.0558	2.4696	0.6205	1	–	–	$16.90^{+2.35}_{-7.51}$	–	0	–	–
COS-S	150.1309	2.4974	1.172	1	–	0.65±0.11	$59.79^{+9.70}_{-9.27}$	–	–	–	–
COS-S	150.1291	2.5168	1.343	1	–	–	$5.73^{+0.62}_{-2.09}$	–	0	–	–
COS-S	150.0871	2.5317	0.8837	2	–	1.84±0.12	$0.10^{+0.03}_{-0.02}$	–	–	–	–
COS-S	150.1869	2.3332	1.0275	1	–	–	$44.93^{+7.32}_{-2.80}$	–	0	–	–
COS-S	150.1828	2.4511	0.718	1	–	–	$1.11^{+0.34}_{-0.17}$	–	–	–	–
COS-S	150.1922	2.2080	0.864	2	–	7.39±1.60	$42.18^{+9.49}_{-3.43}$	–	0	–	–